A Variational Method for Sea Ice Ridging in Earth System Models

Andrew F. Roberts[1,2], Elizabeth C. Hunke[2], Samy M. Kamal[1,3], William H. Lipscomb[4], Christopher Horvat[5], Wieslaw Maslowski[1]

Andrew Roberts, afroberts@lanl.gov

[1]Department of Oceanography, Naval Postgraduate School, Monterey, California, USA

[2]Theoretical Division, Los Alamos National Laboratory, Los Alamos, New Mexico, USA.

[3]Saildrone Inc., Alameda, California, USA.

[4]Climate and Global Dynamics Laboratory, National Center for Atmospheric Research, Boulder, Colorado, USA.

This article has been accepted for publication and undergone full peer review but has not been through the copyediting, typesetting, pagination and proofreading process, which may lead to differences between this version and the Version of Record. Please cite this article as doi: 10.1029/2018MS001395

Abstract. We have derived an analytic form of the thickness redistribution function, Ψ, and compressive strength of sea ice using variational principles. By using the technique of coarse-graining vertical sea ice deformation, or ridging, in the momentum equation of the pack, we isolate frictional energy loss from potential energy gain in the collision of floes. The method accounts for macroporosity of ridge rubble, ϕ_R, and by including this in the state-space of the pack, we expand the sea ice thickness distribution, $g(h)$, to a bivariate distribution, $g(h, \phi_R)$. The effect of macroporosity is for the first time included in the large-scale mass conservation and momentum equations of frozen oceans. We make assumptions that have simplified the problem, such as treating sea ice as a granular material in ridges, and assuming that bending moments associated with ridging are perturbations around an isostatic state. Regardless of these simplifications, the coarse-grained ridge model is highly predictive of macroporosity and ridge shape. By ensuring that vertical sea ice deformation observes a variational principle both at the scale of individual ridges and over the pack as a whole, we can predict distributions of ridge shapes using equations that can be solved in Earth system models. Our method also offers the possibility of more accurate derivations of sea

[5]Institute at Brown for Environment and
Society, Brown University, Providence,
Rhode Island, USA.

ice thickness from ice freeboard measured by space-borne altimeters over polar oceans.

Keypoints:

- We present a framework for sea ice ridging using variational calculus.
- The new framework accounts for the macroporosity of ice ridges and the non-conservation of energy in ridge formation.
- From the statistics of individual ridges, we derive the evolution of the sea ice thickness distribution for the entire pack.

Introduction

Connecting sea ice thickness changes from individual ridging events with regional ice thickness evolution remains a problem in Earth system modeling. This is partly because sea ice mechanics is highly dissipative, and therefore not subject to the energetic constraints of Hamiltonian systems. When sea ice deforms, most of the kinetic energy consumed in the process is not converted to potential energy, but instead is permanently lost from the mechanics through friction and inelastic deformation [*Hopkins et al.*, 1991; *Hopkins*, 1994, 1998]. Predicting the sea ice state, including its velocity, thickness, and fractional ocean coverage (concentration), cannot easily be constrained using the variational principle of stationary action as stated by *Hamilton* [1834, 1835]. If ridging could be constrained in this way, the associated vertical deformation would be minimized over its drift path on the surface of the ocean. Lord Rayleigh proposed a solution for non-conservative systems akin to pack ice [*Strutt*, 1871], enacted as a principle of reduced dissipation [*Virga*, 2015]. However, it is difficult to apply Rayleigh's method without an explicit friction model for sea ice deformation that aggregates many discrete ridging events. As a consequence, basin-scale sea ice models typically rely on an empirical frictional ridging parameterization in their dynamics equations [*Lipscomb et al.*, 2007], rather than on a frictional relation derived from first principles.

In this paper, we derive a mathematical relationship between frictional dissipation during individual ridging events and changes in the distribution $g(h)$ of sea ice thickness h over an area A of pack ice that includes many discrete ridge formations. It constrains the vertical relief of floating morphological features within the pack, including rafts, folds, buckles, rubble fields, ridges and hummocks. These features increase the overall draft

and freeboard of sea ice, and we broadly refer to their construction as ridging. A revised set of sea ice dynamics equations is derived using variational calculus that predicts the spatial distribution of ridges, as well as their shape, porosity, strength and isostatic length scale, providing the foundation for a multi-scale model of sea ice. We contextualize these new developments in section 1. In section 1, we introduce the variational method as it applies to ridging and contrast it with previous empirical approaches to ice deformation. Sections 0.3 and 0.5.3 develop a coarse-grained morphology and frictional approximation for individual ridges that culminates in the emergence of two-dimensional ridge statistics that match observations. Sections 0.7.4 extends the method to large scale sea ice dynamics equations in Earth system models (ESMs), which is the key point of our work. This is our first paper in a series on modeling sea ice thickness; it deals with the theory and equations applicable to ESMs. Planned applications to two ESMs are discussed in the concluding sections of this manuscript.

Motivation and Aim

Vertical sea ice deformation typically occurs along closing leads because it is more efficient for colliding floes to bend, buckle, subduct or overthrust at their edges than to compressively fracture within, unless the ice is thin or ductile [*Weeks*, 2010]. The horizontal flexural and uniaxial tensile strength of first year floes ranges over $\sim 0.1-1.5\,\mathrm{MPa}$ and $\sim 0.2-0.8\,\mathrm{MPa}$, respectively [*Kovacs*, 1996; *Timco and Weeks*, 2010]. By comparison, uniaxial compressive first year ice strength is much greater ($\sim 0.5-5\,\mathrm{MPa}$) [*Mellor*, 1986; *Moslet*, 2007; *Timco and Weeks*, 2010]. Hence, floes seldom break internally under compression, but instead cleave under tension or shear, dividing into smaller floes. Ridges form along the edges of these new plates when they converge, generating blocks of edge

rubble under flexure [*Tucker et al.*, 1984]. Current ESMs lack information about this floe-scale organization of ridges, including their keel depths, sail heights, ridge shapes and spacing. Yet, that information is needed to simulate form drag from winds and currents acting on the pack, a critical momentum exchange in sea ice models [*Tsamados et al.*, 2014; *Martin et al.*, 2016].

A large fraction of kinetic energy is lost from friction within ridge rubble as part of floe tectonics. This loss is in addition to the kinetic energy expended when colliding floes fracture into virgin rubble. The scale of the resulting rubble blocks is correlated with the original thickness of the parent sheet, h_F, from which the debris is calved [*Tucker et al.*, 1984; *Strub-Klein and Sudom*, 2012]. Block sizes may be scale invariant up to a limit imposed by h_F [*Weiss*, 2001], which contributes to heterogeneous voids in the ridge mélange, as seen for two Beaufort Sea ridges in Figure 1. However, observations are seldom possible of the evolution of ice keels and sails riddled, respectively, with waterlogged and aerated voids. This makes contribution of the voids to sea ice energetics difficult to quantify in ESMs. Instead, measurements of permeable spaces within ridges are usually quantified in terms of the bulk porosity ϕ_R of their final deformed state.

Nuclear magnetic resonance tomography indicates that the macroporosity between keel blocks can exceed 40% [*Nuber et al.*, 2013], as do sectional and incisional ridge surveys [*Bowen and Topham*, 1996; *Høyland*, 2007]. These measurements typically yield a lower bulk macroporosity for entire ridges of between $\sim$20$-$30% due to refreezing between blocks near the waterline, otherwise known as ridge consolidation [*Leppäranta and Hakala*, 1992; *Timco and Burden*, 1997; *Johnston and Barker*, 2000; *Strub-Klein and Sudom*, 2012]. ϕ_R often exceeds the bulk microporosity, ϕ_μ, of first-year ridge blocks caused by brine

and air pockets within their crystal structure, where ϕ_μ typically ranges between $\sim$2 and 12% in mildly-frigid to near-melting conditions [*Kovacs*, 1997; *Pringle et al.*, 2009]. To our knowledge, there is no prognostic model for ϕ_R applicable to ESMs, even though it is a fundamental state variable affecting kinetic energy loss, potential energy gain, and therefore the global momentum and mass balance of sea ice.

To address this problem, the evolution of ridge porosity must be considered in ESMs. We accomplish this by expanding the typical sea ice thickness distribution, $g(h)$, to a bivariate distribution of thickness and macroporosity $g(h, \phi_R)$. The bulk density ρ of intact sea ice is then more clearly defined as a function only of the microporosity of rubble and floes, ϕ_μ, their salinity, s, and enthalpy, ε, as used in purely thermodynamic models of saline ice [e.g. *Turner and Hunke*, 2015]. The sea ice density $\rho{=}\rho(\phi_\mu, s, \varepsilon)$ can then be used in conjunction with ϕ_R to determine the bulk density of an area of ridged sea ice, $\rho(1-\phi_R)$, and hence its draft h_d and freeboard h_f in large scale models. Although isostasy need not apply [*Melling et al.*, 1993; *Doble et al.*, 2011; *Geiger et al.*, 2015], it can be used to estimate h_d and h_f just as in models that only resolve $g(h)$ as described by *Lipscomb et al.* [2007]. The classic sea ice thickness distribution $g(h)$ is then simply an integral of $g(h, \phi_R)$:

$$g(h) = \int_0^1 g(h, \phi_R)\, d\phi_R. \tag{1}$$

In this scenario, the variable $h{\in}[0, \infty)$ still defines the vertical distance from the bottom of a column of sea ice to its upper interface, but now that column may contain gaps between ridged ice blocks when $\phi_R{\in}[0, 1)$ is included in the state space. This bivariate framework is thus a main component of future multi-variate sea ice state functions for

ESMs that incorporate floe-scale effects [e.g. *Horvat and Tziperman*, 2015; *Roach et al.*, 2018].

The evolution of $g(h, \phi_R)$ can be used to describe mass conservation aggregated over many simultaneous ridging events in a similar way to $g(h)$. The aim of this paper is to derive from first principles a method to accomplish this. *Thorndike et al.* [1975] introduced a mechanical redistribution function Ψ for the evolution of $g(h)$, which is described in Lagrangian coordinates as:

$$\frac{dg}{dt} = \Theta + \Psi - g(\nabla \cdot \dot{\boldsymbol{x}}). \tag{2}$$

$\dot{\boldsymbol{x}}$ is the aggregated velocity of the material area $A(\boldsymbol{x})$ with a sea surface path $\boldsymbol{x}$ illustrated in Figure 2 for time t. Θ is condensed from *Hibler* [1980] to describe evolution of $g(h)$ due to freezing and melting. Herein, we will adapt (2) to the bivariate distribution $g(h, \phi_R)$ and thus derive a new expression for Ψ, first for an individual ridge, and then for fields of developing ridges, i.e. the full sea ice surface. This effort makes available local information about ridge shapes, spacing, and porosities to the large-scale equations for sea ice momentum, flux exchanges and marine biogeochemistry. We set aside development of Ψ's bivariate thermodynamic analogue, Θ, for later work. A postscript table of mathematical notation may be referenced while reading this paper.

Methods

0.1. The Variational Method for Sea Ice Mechanics

The redistribution function for $g(h)$ developed by *Thorndike et al.* [1975] used the energy method of *Rothrock* [1975] to quantify frictional energy loss in terms of the potential energy gain of rubble ridged above and below the waterline. Rothrock's method has subsequently been adapted to many basin-scale sea ice models, including by *Hibler* [1980]

, *Flato and Hibler* [1995], *Bitz et al.* [2001], *Zhang and Rothrock* [2003], *Lipscomb et al.* [2007], *Vancoppenolle et al.* [2009] and *Castro-Morales et al.* [2014]. It implicitly makes use of the principle of virtual work, and in this paper we will make explicit use of that principle. We will first introduce important variational principles of sea ice mechanics, and then place Rothrock's energy method in that context. For detailed explanations of the methods that we apply here, we refer the reader to texts by *Lanczos* [1970], *Bedford* [1985] and *Cassel* [2013].

Before proceeding, we define the Lagrangian coordinates in which we will be working, and the associated mechanics term. For a field of ice, the Lagrangian path is defined as a function $\boldsymbol{x} = \chi(\boldsymbol{X}, t)$ over the material area $A(\boldsymbol{x})$ where $\boldsymbol{X}$ is a reference coordinate to which a moving parcel may be mapped at any time between the initial and final time of its passage, t_i to t_f (Fig. 2). We should strictly write $g(h)$ and $g(h, \phi_R)$ with reference to the path, $g(h, \boldsymbol{x})$ and $g(h, \phi_R, \boldsymbol{x})$, but avoid that cumbersome notation where possible. The Cauchy internal sea ice stress tensor $\boldsymbol{\sigma}{=}(\sigma_{mn})$ for $m, n = 1, 2$ traditionally used with Eulerian coordinates takes the form $\bar{\boldsymbol{\sigma}} = J\boldsymbol{\sigma}\boldsymbol{J}^{-T}$ in our Lagrangian reference frame, where $J = \det(\boldsymbol{J})$ is the Jacobian, and $\boldsymbol{J} = \partial\boldsymbol{x}/\partial\boldsymbol{X}$. There is little practical difference between the strain tensor in the reference coordinate $\boldsymbol{X}$ and on the path $\boldsymbol{x}$ so that we may universally define it as $\boldsymbol{\epsilon}{=}(\epsilon_{mn})$, where $\epsilon_{mn}{\approx}\frac{1}{2}(u_{m,n} + u_{n,m})$ for the displacement vector $\boldsymbol{u}(\boldsymbol{X})$. Contrary to other sea ice literature, $\boldsymbol{u}$ is not drift velocity. $\epsilon_I = \epsilon_{mm}$ is tensile strain, $\epsilon_{II} = \sqrt{({\epsilon_I}^2 - 4|\epsilon_{mn}|)}$ is shear strain, and pure compression occurs when $\theta = \pi$, given $\theta = \arctan(\epsilon_{II}/\epsilon_I)$. Analogous definitions for strain rate $\dot{\boldsymbol{\epsilon}} = (\dot{\epsilon}_{mn})$ apply for divergence and rate of shear.

By applying the variational method to sea ice, we are not only able to analyze the passage of ice along one particular track between t_i to t_f, such as the solid red path in Figure 2. We can also understand constraints on ice mechanics over an infinite number of possible paths between the start and end points $\boldsymbol{x}_\mathrm{i}$ and $\boldsymbol{x}_\mathrm{f}$, including the alternative dotted paths in Figure 2. Following Lagrange, we signify a test of all possible paths between $\boldsymbol{x}_\mathrm{i}$ and $\boldsymbol{x}_\mathrm{f}$ with the first order variational vector $\delta\boldsymbol{x}$. This symbol from variational calculus is not to be confused with the discretization $\Delta\boldsymbol{x}$ of infinitesimals often used in Earth system modeling. In our work, we need only explore variations in $\boldsymbol{x}$ to the first order, because that is sufficient to describe the energetics of sea ice mechanics.

The change in kinetic energy of an area A of drifting sea ice results from internal work from stress between floes, as well as external work from traction along its perimeter C and body forces applied over $\boldsymbol{x}$ (Fig. 2). This may be expressed as a time integral for arbitrary variations in the Lagrangian path $\boldsymbol{x}$:

$$\int_{t_\mathrm{i}}^{t_\mathrm{f}} \int_A \Big(- m\,\frac{d\dot{\boldsymbol{x}}}{dt} + \boldsymbol{F}_\mathrm{b} + \nabla\cdot\bar{\boldsymbol{\sigma}}\Big)\cdot\delta\boldsymbol{x}\; dA\; dt \;+ \int_{t_\mathrm{i}}^{t_\mathrm{f}} \oint_C \Big(\boldsymbol{F}_\mathrm{t} - \bar{\boldsymbol{\sigma}}\boldsymbol{N}\Big)\cdot\delta\boldsymbol{x}\; dS\; dt = 0 \quad (3)$$

In the left-hand parentheses in (3), m is the mass per unit area and $\boldsymbol{F}_\mathrm{b}$ is the body stress acting on the continuum of sea ice within A. Inside the right-hand parentheses, the traction stress $\boldsymbol{F}_\mathrm{t}$ surrounding A is balanced by internal stress $\bar{\boldsymbol{\sigma}}\boldsymbol{N}$ normal to S, and so the line integral in (3) vanishes. The body stress arises from sea surface tilt $\nabla\eta$, wind and ocean current stress, $\boldsymbol{\tau}_a$ and $\boldsymbol{\tau}_w$, and Coriolis acceleration, given the upward unit normal vector $\mathbf{k}$ and Coriolis parameter f:

$$\boldsymbol{F}_\mathrm{b} = \boldsymbol{\tau}_a + \boldsymbol{\tau}_w + m\mathrm{f}\,\mathbf{k}\times\dot{\boldsymbol{x}} - m\hat{\mathrm{g}}\nabla\eta. \quad (4)$$

$\hat{\mathrm{g}}$ is standard gravity. The left-hand parentheses in (3) encapsulates Newton's second law for sea ice in a Lagrangian reference frame, which must sum to zero in order for the scalar product with the first order variation $\delta\boldsymbol{x}$ to vanish. This is the method by which one derives the sea ice momentum equation based on energetics. Even though there is frictional loss in sea ice dynamics via internal stress, a variational principle still applies. That is, the sea ice momentum equation remains true regardless of the drift path of an area of the pack, and therefore the sum of the terms in the left hand parentheses remains stationary when integrated over any path, and observes a principle of least action.

In our case, we are concerned only with changes in sea ice kinetic energy due to internal stress. We may disregard body stress, itself a non-conservative term, because significant spatial gradients in $\boldsymbol{F}_{\mathrm{b}}$ typically occur over greater horizontal scales than are relevant to our problem. Instead we need only consider traction forces, whereafter equation (3) reduces to a simpler form:

$$0 = \int_{t_{\mathrm{i}}}^{t_{\mathrm{f}}} \int_A \left(\nabla \cdot \bar{\boldsymbol{\sigma}} - m \frac{d\dot{\boldsymbol{x}}}{dt} \right) \cdot \delta\boldsymbol{x} \; dA \; dt \tag{5}$$

This may be restated as Hamilton's principle of least action for continuum mechanics [*Bedford*, 1985],

$$\int_{t_{\mathrm{i}}}^{t_{\mathrm{f}}} \int_A \left(\delta\mathcal{T} + \delta\mathcal{W} \right) \; dA \; dt = 0, \tag{6}$$

where $\mathcal{T}$ is kinetic energy per unit area of the pack, otherwise known as kinetic energy density, and $\mathcal{W}$ is equivalently the work density over A. The δ symbol refers to variations in $\mathcal{T}$ and $\mathcal{W}$ depending on the path, for which $\delta\mathcal{T} = m\,(d\dot{\boldsymbol{x}}/dt) \cdot \delta\boldsymbol{x}$. The term $\delta\mathcal{W} = -(\nabla \cdot \bar{\boldsymbol{\sigma}}) \cdot \delta\boldsymbol{x}$ is called the *virtual work density*. Part of the virtual work performed along an arbitrary path goes toward an increase in thickness due to ridging, and thus to a *virtual potential energy density*, denoted $\delta\mathcal{V}$. The rest is lost to friction and inelastic deformation.

The challenge in representing ridging in ESMs has been to determine the kinetic energy lost from the system, $\delta\mathcal{W} - \delta\mathcal{V}$, and thus to correctly model changes in sea ice thickness. Hamilton's principle alone does not help us with that problem.

0.2. An Empirical Approach to Modeling $g(h)$

Without a variational constraint on the kinetic energy lost during ridging, *Rothrock* [1975] and *Thorndike et al.* [1975] approached the problem empirically. They simplified the problem, and assumed ridged ice to be equally as porous as undeformed material, giving rise to the distribution $g(h)$. They disallowed ridge crumbling (i.e. $\delta\mathcal{V} \geq 0$) and assumed isostasy everywhere, permitting an approximation for energy loss:

$$\delta\mathcal{W} = C_f\, \delta\mathcal{V} \tag{7}$$

Here, $C_f \in [1, \infty)$ is a constant that accounts for dissipation [*Lipscomb et al.*, 2007], and $(C_f - 1)/C_f$ is the fraction of kinetic energy lost, which computer simulations suggest may account for 90-95% of all ridging work [*Hopkins*, 1994, 1998]. Equation (7) is used in many models to parameterize ridging, typically with $C_f = 17$, yet its accuracy is questionable [*Ungermann et al.*, 2017], and it is difficult to justify theoretically.

Thorndike et al. [1975] aggregated the change in potential energy over A in terms of an initial distribution of thickness $a(h_\mathrm{i}, \boldsymbol{x}_\mathrm{i})$ for the area of ice within $g(h_\mathrm{i})$ that is deforming, which shifts to a thicker final state $a(h_\mathrm{f}, \boldsymbol{x}_\mathrm{f})$ over $\Delta t = t_\mathrm{f} - t_\mathrm{i}$, using the empirical pressure ridging mode:

$$\omega_R(h, \boldsymbol{x}) = \lim_{\Delta t \to 0} \left(\frac{a(h_\mathrm{f}, \boldsymbol{x}_\mathrm{f}) - a(h_\mathrm{i}, \boldsymbol{x}_\mathrm{i})}{-\int_0^\infty \big(a(h_\mathrm{f}, \boldsymbol{x}_\mathrm{f}) \, - \, a(h_\mathrm{i}, \boldsymbol{x}_\mathrm{i})\big)\, dh} \right). \tag{8}$$

Further explanation of this term may be found in *Lipscomb et al.* [2007]. $\omega_R(h, \boldsymbol{x})$ conserves area ($-\int_0^\infty \omega_R\, dh{=}1$) and ice volume ($\int_0^\infty h\, \omega_R\, dh{=}0$), and is used to estimate

the change in potential energy density $\mathcal{V}$ with variations in tensile strain $\delta\epsilon_I$, as dictated by variational calculus:

$$\int_{t_\mathrm{i}}^{t_\mathrm{f}} \delta\mathcal{V}\, dt \approx \int_{t_\mathrm{i}}^{t_\mathrm{f}} \frac{\rho\,\Delta\rho\,\hat{\mathrm{g}}}{2\,\rho_w}\Big(\int_0^\infty h^2\,\omega_R(h,\boldsymbol{x})\,dh\Big)\,\delta\epsilon_I\,dt. \tag{9}$$

ρ and ρ_w are ice and water density, respectively, and $\Delta\rho{=}\rho_w{-}\rho$. We have limited (9) to the purely compressive case, where it is the variational equivalent of equation 8 in *Rothrock* [1975] when $\theta{=}\pi$. The redistribution function for all θ is given by

$$\Psi = \dot{\underline{\epsilon}}\,\big[\xi(\theta)\,\omega_R(h,\boldsymbol{x}) + \big(\xi(\theta)+\cos\theta\big)\hat{\delta}(h)\big], \tag{10}$$

for the strain rate magnitude $\dot{\underline{\epsilon}}{=}\sqrt{(\dot{\epsilon_I}^2{+}\dot{\epsilon_{II}}^2)} \geq 0$, where $\theta{=}\arctan(\epsilon_{II}/\epsilon_I)$ is synonymous with $\arctan(\dot{\epsilon}_{II}/\dot{\epsilon}_I)$ for infinitesimal strain. $\hat{\delta}(h)$ is a Dirac delta function and $\xi(\theta)$ describes the extent to which ridging occurs in conditions of combined convergence and shear as determined by the yield criteria [*Lipscomb et al.*, 2007]. It may be shown from (5) and (6) that $\delta\mathcal{W} = J\boldsymbol{\sigma}:\delta\boldsymbol{\epsilon}$, so that (7) and (9) combine to give the compressive strength P of sea ice in the form originating from *Rothrock* [1975],

$$P = C_f\,\frac{\rho\,\Delta\rho\,\hat{\mathrm{g}}}{2\,\rho_w}\int_0^\infty h^2\,\omega_R(h,\boldsymbol{x})\,dh. \tag{11}$$

In most representations of large-scale sea ice dynamics, P appears as a coefficient in the constitutive relation $\boldsymbol{\sigma} = P\boldsymbol{f}$ given the yield criterion $\boldsymbol{f} = f_{mn}(\dot{\epsilon}_{jk})$ and $j,k = 1,2$ [see *Hunter*, 1983, for further explanation of $\boldsymbol{f}$ expressed in this brief way].

Ungermann et al. [2017] demonstrated that this representation of P reduced the accuracy of Arctic sea ice simulations relative to simpler parameterizations that do not account for sea ice energetics. That result may derive from several limitations of the empirical method. First, specifying friction in (11) with a universal constant, C_f, may oversimplify the complexity of kinetic energy loss during ridging. Second, the empirical ω_R requires

a priori knowledge of the initial sub-distribution $a(h_\mathrm{i}, \boldsymbol{x}_\mathrm{i})$ and its final state $a(h_\mathrm{f}, \boldsymbol{x}_\mathrm{f})$. Conservative systems may be solved using an initial and final state, but non-conservative systems, including pack ice mechanics, must be treated strictly as initial value problems [*Galley*, 2012]. Therefore, the final ridged state $g(h_\mathrm{f})$ should be predicted in terms of the initial condition $g(h_\mathrm{i})$, the path $\boldsymbol{x}$ and velocity $\dot{\boldsymbol{x}}$. *Godlovitch et al.* [2011] and *Toppaladoddi and Wettlaufer* [2015] have explored physical analogues for ridging that describe the transition of $g(h_\mathrm{i})$ to the *probable* final thickness state $g(h_\mathrm{f})$. But the macroporous influence on deforming ice remains to be considered, even when ridging is posed as an initial value problem.

0.3. Modeling $g(h, \phi_R)$ by Coarse-Graining

In this study, we derive a constraint for $\delta\mathcal{W}$ using a variational method that results in a redistribution function Ψ for $g(h, \phi_R)$. To do this, we seek a solution to the Euler-Lagrange equation for ridging, which equates to Newton's second law in equation (5), and against which we test for variations over the path $\delta\boldsymbol{x}$:

$$\partial_\chi \frac{\partial \mathcal{L}}{\partial(\partial_\chi \boldsymbol{x})} - \frac{\partial \mathcal{L}}{\partial \boldsymbol{x}} - \boldsymbol{\mathcal{Q}} = m\,\frac{d\dot{\boldsymbol{x}}}{dt} - \nabla\cdot\bar{\boldsymbol{\sigma}} = 0. \tag{12}$$

$\mathcal{L} = \mathcal{T} - \mathcal{V}$ is the Lagrangian density, and it represents the conversion of kinetic to potential energy during ridging, a conservative and scalar exchange. The non-conservative internal ice force per unit area, $\boldsymbol{\mathcal{Q}}$, is as yet unknown, and reference between $\boldsymbol{X}$ and the Lagrangian path $\boldsymbol{x}$ within the continuum is provided by $\partial_\chi \boldsymbol{x} = \partial\boldsymbol{x}/\partial t + \partial\boldsymbol{x}/\partial\boldsymbol{X}$. The advantage of solving the Euler-Lagrange equation is that we are able to describe conservative interactions during ridging purely in terms of scalars $\mathcal{T}$ and $\mathcal{V}$. This reduces the problem to a single vector term, $\boldsymbol{\mathcal{Q}}$, the non-conservative component.

Using a different mathematical framework to ours, *Rothrock* [1975] quantified $\boldsymbol{\mathcal{Q}}$ by deriving it in terms of pressure ridging, without horizontal shear, thereby determining the compressive strength, P. He then expanded his solution to include shear stress by way of the yield criterion, $\boldsymbol{f}$. We adopt a similar method, simplifying our Euler-Lagrange equation to a one-dimensional problem aligned in the direction $\hat{x}$ of pure compressive stress $\sigma_{\hat{x}}$. In this context, the non-conservative force per unit area is $\boldsymbol{\mathcal{Q}}_{\hat{x}}$ and derivatives with respect to the reference coordinate $\boldsymbol{X}$ disappear:

$$\frac{d}{dt}\frac{\partial \mathcal{T}}{\partial \dot{\hat{x}}} - \frac{\partial \mathcal{V}}{\partial \hat{x}} - \boldsymbol{\mathcal{Q}}_{\hat{x}} = m\frac{d\dot{\hat{x}}}{dt} - \frac{\partial \sigma_{\hat{x}}}{\partial \hat{x}} = 0. \tag{13}$$

In this context, ridging is a straightforward mechanical interaction: a decrease in kinetic energy density $\mathcal{T}$, is countered by an increase in potential energy density $\mathcal{V}$, and a one-dimensional resistive non-conservative stress $\boldsymbol{\mathcal{Q}}_{\hat{x}}$, as seen in the left-hand side of (13). Our method departs from previous work in the way in which we quantify $\mathcal{V}$ and $\boldsymbol{\mathcal{Q}}_{\hat{x}}$, and in the way we account for shear in ridge formation.

To derive an estimate for $\boldsymbol{\mathcal{Q}}_{\hat{x}}$ for the entire sub-grid-scale area $A(\boldsymbol{x})$, we 'coarse-grain' ridge formation along $\hat{x}$ and test our solution against the variation $\delta\hat{x}$. Coarse-graining is a method of reducing complex interactions between particles to a system of simplified interactions between clusters of particles. For instance, it is used to model protein systems by treating inter-molecular interactions distinctly from intra-molecular evolution [e.g. *Noid et al.*, 2008; *Kmiecik et al.*, 2016]. This facilitates multi-scale modeling of a material, and in our case, it allows complex ridged regions to be simplified within $A(\boldsymbol{x})$. Each ridging space along $\hat{x}$ has a local ridge thickness distribution $g_R(h, \phi_R)$ which can be treated individually, and the surrounding areas may be considered as floe ice, or at least non-deforming material. The mechanics of each ridging space is analyzed using the continuum

approximation in (13) for which there are precedents in the literature. Once we have established an inexpensive model of individual ridges, we then derive the related equations and the statistics they produce for collections of ridges. This type of coarse-graining is unrelated to the method used by *Marsan et al.* [2004] to understand scaling in horizontal sea ice deformation.

The coarse-grained ridging model described next draws on mechanical descriptions of ridging by *Zubov* [1945], *Parmerter and Coon* [1972], *Mellor* [1980], *Hopkins et al.* [1991], *Hopkins* [1994, 1998], *Timco et al.* [2000], *Heinonen* [2004], and *Kuuliala et al.* [2017]. We also utilize statistical studies of ridges. The submarine survey of *Davis and Wadhams* [1995] is particularly significant because it collates measurements from a large number of ridges (729). In that study, cross-sectional keel profiles were sampled by HMS Superb during May 1987 with upward-looking sonar [*Wadhams*, 1988], and oriented relative to the submersible's track using sidescan sonar. Keel shapes were obtained over six transects ∼44-49 km long, located in the vicinity of the North Pole and Lincoln Sea, and in Fram Strait. Statistical relations of ridges from that work are corroborated by Baltic, Weddell Sea, and Arctic Ocean aerial surveys [*Lewis et al.*, 1993; *Tan et al.*, 2012; *Petty et al.*, 2016]. We use *Melling and Riedel* [1995, 1996] extreme keel depth relations from profiling sonars moored in the Beaufort Sea each winter from 1990 to 1992. Finally, sail height distributions and ridge porosity statistics are used from *in-situ* ridge studies from the 1970's to the current decade. These include the Prudhoe Bay compilation of 84 ridges by *Tucker et al.* [1984], and observations of 112 and more than 300 first-year boreal ridges by *Timco and Burden* [1997] and *Strub-Klein and Sudom* [2012], respectively.

Coarse-Grained Ridge Morphology

0.4. Polygonal Approximation

The polygonal frame in Figure 3 represents our coarse-grained morphology of ridges. The scaled cross-section of the keel and sail relief is oriented perpendicular to the ridge line, or keel crest, between two floating parent sheets, designated F_a and F_b in the plan view in Figure 4a, akin to the idealization of *Ekeberg et al.* [2015]. Ice and snow volumes within ridges are formed from these level, isostatic floes, each assumed to have locally unvarying thickness. They provide boundary conditions for the ridge, so that the minimum ridge thickness either side of the sail peak is identical to that of the parent sheets feeding the edges of the deforming zone, as seen in Figure 5. We assume that bending moments in floes feeding each ridge result in fracture of the floes, as first noted by *Makarov* [1901], and our ridge morphology reflects the final state of the fractured ice pile after the bounding floes have relaxed back to their isostatic state. Following from *Parmerter and Coon* [1972], this permits the assumption that the ridge structure is isostatic as a whole, and therefore the sail and keel peaks are horizontally aligned. Columns of porous ice within the ridge will typically violate Archimedes' Principle, so that the isostatic length scale is quantized at the keel half-width, $L_K/2$. Following *Zubov* [1945], the ridge has a 'coefficient of filling' equivalent to $1 - \phi_R$, where ϕ_R is the bulk macroporosity of the structure.

0.4.1. Physical Description

Horizontal shearing is a boundary condition imposed on the coarse-grained ridge by the angle $\theta_R = \arctan(\epsilon_{R_{II}}/\epsilon_{R_I})$ at the ridge line dividing colliding floes, annotated in Figure 4. This is the ridge-scale analogue of θ introduced in section 0.1 for local shear $\epsilon_{R_{II}}$, and expansive strain ϵ_{R_I}, where a pressure ridge represents the special case $\theta_R = \pi$ (Figure 4a). Ridge building occurs when $\pi/2 < \theta_R \leq \pi$. We orient orthogonal coordinates

of the ridge $\hat{\boldsymbol{x}}(\hat{x}, \hat{y}, \hat{z})$ so that $\hat{x}$ is parallel to the large-scale horizontal principal axis aligned with divergence $\dot{\epsilon}_I$. Therefore ridges are formed from convergent horizontal floe velocities $\hat{v}_{F_a}(\hat{x}) \geq 0$ and $\hat{v}_{F_b}(\hat{x}) \leq 0$ seen in Figures 4 and 5. The $\hat{y}$ axis is orthogonal to $\hat{v}_{F_a}$ and $\hat{v}_{F_b}$ and aligned with the horizontal principal axis $\dot{\epsilon}_{II}$. The coordinate $\hat{z}$ is aligned with ridge thickness and orthogonal to $\hat{x}$ and $\hat{y}$ and $\hat{\boldsymbol{x}}(\hat{x}, \hat{y}, \hat{z})$ traces the horizontal path $\boldsymbol{x}$ of the large scale dynamics. Whereas the idealization in Figure 4 presents straight-sided floe edges for clarity, θ_R may freely vary along a ridge line.

Vertical relief in Figure 3 is described in terms of ridge half-widths in a similar manner to *Davis and Wadhams* [1995]. Each half-ridge shape may be described in 10 variables: (1) thickness of level ice below the waterline, h_{F_d}; (2) thickness of level ice plus snow above the waterline, h_{F_f}; (3) mean thickness of deformed ice below the waterline *not including porous spaces*, h_{R_d}; (4) mean thickness of deformed ice plus snow above the waterline *not including porous spaces*, h_{R_f}; (5) maximum sail height, H_S, shared by both sides of the ridge; (6) cross-sectional sail half-width, $L_S/2$; (7) maximum keel depth, H_K, also shared by both sides of the ridge; (8) cross-sectional keel half-width, $L_K/2$; (9) bulk macro-porosity of the ridge, ϕ_R; and (10) the principal strain angle θ_R. Notation is further explained in the postscript, where subscript F represents floe ice or parent material feeding a ridge, subscript R denotes ridging ice, and subscripts f, d and s indicate freeboard, draft, and snow, respectively.

0.4.2. Archimedean Approximation

A full mathematical description of the ridge morphology is provided in appendix A, and here we summarize the physical constraints applied to the morphology. Archimedes' principle applies across ridge halves as a whole, but individual columns of ice within the

structure may not necessarily be isostatic. Mass and volume are conserved, leading to expressions for both horizontal tensile strain and divergence across the ridge, ϵ_{R_1} and $\dot{\epsilon}_{R_1}$ (appendix A). A fraction of snow is lost to the ocean during ridging, specified by an equal areal volume of snow on ridges as on floes ($h_{R_s} = h_{F_s}$). Finally, we constrain the shape of a ridge so that the angle of repose of sails and keels are equal, $\alpha_S = \alpha_K$ (Figure 3). We refer to these identical angles in terms of the half-ridge angle of repose on the compressional axis, α_R, and horizontal shear, θ_R: $\cot \alpha_K = \cos(\pi - \theta_R) \cot \alpha_R$. As a consequence, we are able to describe the horizontal and vertical extent of floating deformations, L_S, L_K, H_S, and H_K, in terms of the parent ice and snow thickness, h_F and h_{F_s}, and its tensile strain, porosity, compressional angle of repose, and horizontal shearing angle, ϵ_{R_I}, ϕ_R, α_R, and θ_R respectively.

The floating state of each ridge is independent of floe velocities $\hat{v}_{F_a}$ and $\hat{v}_{F_b}$, stemming from work by *Parmerter and Coon* [1972] and *Hopkins et al.* [1991], where ridge shapes were demonstrated to mature to roughly triangular keel and sail slopes in isostatic equilibrium. *Rothrock* [1975] similarly described ridges in terms of their final static states, which allowed him to make frictional loss independent of velocity in equation (7), similar to the approach we will use. But contrary to that study, we do not assume that the entire pack is isostatic nor imporous, only that each ridge half as a unit is isostatic, along with the non-deforming parts of the parent sheet.

0.5. Fundamental Properties

Before deriving equations that relate the ridge state space ϵ_{R_I}, ϕ_R, and α_K to frictional loss, it is important to understand the advantages and limitations of this coarse-grained morphology for its intended application in large-scale models. This is done with the help

of scaled orthographic sections, or 'ridgegraphs', that provide solutions to equations 1 to 16, and permit comparisons to be made between different ridge states. Table 1 lists the constants used for snow, saline ice and sea water.

0.5.1. Isostatic Shape

The apparently simple coarse-grained morphology introduced in section 0.4 provides a surprisingly general approximation of deformed rubble. Whereas real ridges have fractal profiles [*Key and Mclaren*, 1991; *Melling et al.*, 1993], such detail is not required here because the polygonal frame is a sufficient building block for kilometer-scale ice dynamics. Figure 5 illustrates this point, where randomly generated pressure ridges (gray) share the same centroid, waterline and half-ridge volume densities (V_R) as the polygonal isostatic quanta (orange outline). The polygonal approximation integrates fine-grained ridge roughness and acts as a metric of ridge extremities. Figure 5a demonstrates that the extremities, H_K, H_S, and L_K, are all functions of isostasy. This example uses boundary conditions $h_F = 2.0\,\mathrm{m}$ and $h_{F_s} = 0.3\,\mathrm{m}$, corresponding to spring modal ice thickness and snow cover in parts of the recent Beaufort Sea [*Haas et al.*, 2010; *Webster et al.*, 2014]. The ridge is mildly strained ($\epsilon_{R_I} = -1/3$) and 20% porous, with an angle of repose $\alpha_K = 22°$ used by *Tsamados et al.* [2014] to model form drag, close to the *Davis and Wadhams* [1995] observed mean (23.2°). In this case, $\alpha_K = \alpha_R$ because there is no horizontal shear ($\theta_R = \pi$).

Asymmetric ridge shapes may occur when thin ice converges against a thick floe, as represented in the discrete element modeling of *Hopkins* [1994]. Figure 5b presents this scenario for a snowless parent ice sheet 0.5 m thick colliding with the baseline floe taken from Figure 5a. Bulk porosity is identical through the ridge, as well as the angle of shear,

because these are ridge-wide properties. The thick floe has a much smaller horizontal ridge strain ($\epsilon_{R_I1} = -0.33$), than the thin floe ($\epsilon_{R_I2} = -0.83$) in order for them to share the same keel draft and sail height. There are important limits on the ridge shape and relative strains of the two parent sheets that we derive in section 0.5.3. Meanwhile, we confine our ridgegraphs to symmetric cases, but the half-ridge shapes within them are applicable to asymmetric combinations within the pack.

Spectrums of keel shapes are possible in the coarse-grained state space, and may be compared with sonar measurements. The angle of keel repose, irrespective of shear, is $\alpha_K = \arctan(2(H_K - h_{F_d})/L_K)$ (see equation 14). This compares with keel profiles of *Davis and Wadhams* [1995], who measured α_K relative to the baseline draft, h_{F_d}, following *Wadhams and Davy* [1986]. They then expressed it as a function of $L_K/(2H_K)$, which is the keel half-width-to-draft ratio. This *Davis and Wadhams* [1995] analysis is reproduced in Figure 6, and our coarse-grained solution is overlaid as a solid blue line for the bounding case $H_K \gg h_{F_d}$ where the level ice draft is much less than the keel, effectively the case of $h_{F_d} = 0$. The dotted blue line is the coarse-grained case where the parent sheet draft is half as much as the keel, and indicates the observational range of the keel-to-level-ice draft ratio. Both the solid and dotted blue lines indicate that the analytic cotangent relationship, $L_K = 2\,(H_K - h_{F_d})\cos(\pi - \theta_R)\,\cot\alpha_R$ in (14) better explains keel measurements than an empirical exponential fit first proposed by *Davis and Wadhams* [1995]. The color shading in Figures 6a and 6b presents variational solutions to ridge porosity depending on different amounts of shear (θ_R), discussed later.

Simplifications made to the treatment of snow ($h_{R_s} = h_{F_s}$) and sail shape ($\alpha_S = \alpha_K$) have little morphological impact, demonstrated in a supplement to this manuscript. By con-

trast, ridge shapes are highly sensitive to bulk porosity (ϕ_R), compression ($-\epsilon_{R_I}$) and angle of repose (α_R), as well as horizontal shear (θ_R). Of these, the dependence of large scale ice mechanics on macroporosity has remained enigmatic, but the coarse-grained morphology is able to shed light on its role.

0.5.2. Porosity and Strain

Ridge porosity transforms the sea ice thickness distribution in a similar way to strain. This effect is best understood using the bivariate thickness distribution of individual ridges, $g_R(h, \phi_R)$, which is normalized over the width in the compressional direction, $\hat{L}_K{=}L_K/\cos(\pi - \theta_R)$, as derived in appendix B. Each ridge has a step distribution for $g_R(h, \phi_R)$, illustrated in Figure 7. The h-coordinate of the intermediary $g_R(h, \phi_R)$ step depends on the angle of sail repose relative to that of the keel, but the influence of ridge porosity relative to strain remains the same irrespective of this constraint. Figure 7 presents four distributions corresponding to the ridgegraph in Figure 8 for our chosen sail shape $\alpha_S = \alpha_K$. Pressure ridges (a) through (d) use the same baseline parent sheet and angle of repose as in Figure 5a ($h_F = 2.0\,\mathrm{m}$, $h_{Fs} = 0.3\,\mathrm{m}$, $\alpha_R = 22°$, $\theta_R = 180°$), and differ only by porosity and strain. Transformation of the imporous ridge in (a) by increasing strain in (b), or increasing porosity in (c), stretches $g_R(h, \phi_R)$ along the h-axis and decreases the relative proportion of different thicknesses within the ridge (Figure 7). In both cases (b) and (c), the ridge becomes deeper, higher and wider than the initial impervious pile (Figure 8).

While strain's influence on ridge shape is intuitive, the analogous effect of ridge porosity may seem less obvious. By increasing strain, ice mass is added to a ridge so that all of its extremities expand. Increasing porosity has the same morphological impact, but adds

no extra mass to ridges, only volume. The relative amounts of expansion in the vertical and horizontal occurs because the ice mass is floating. A potential consequence of this is presented in Figures 7d and 8d, where the ridge has zero strain but acquires 20% porosity from fracturing ice. Vertical relief must result, and a slender ridge appears in the statically-stressed ice, with an associated small increase in potential energy of the pack. In this case, there are no associated horizontal kinematics, since there is no convergence and $\hat{v}_{F_a} = \hat{v}_{F_b} = 0$. Yet, a ridge is still created, and there is an energetic cost due to potential energy gain in addition to the work of fracture incurred by breaking ice into rubble. We will demonstrate in section 0.5.3 that a reasonable friction model precludes this case.

Still, the expansionary property of macroporosity has largely been overlooked in sea ice models. For example, the *Tsamados et al.* [2014] and *Martin et al.* [2016] diagnostic form-drag parameterization assumes that ridges are 20% porous (although they designated macroporosity as Zubov's coefficient of filling: $1-\phi_R = 0.8$). In these studies, ϕ_R was applied diagnostically to imporously-ridged material generated only from strain. Using our coarse-grained morphology, it can be seen that this effectively inflates the keel depth, sail height and ridge widths as compared to the actual thickness distribution $g(h)$. Figures 8a and 8c demonstrate the effect of increasing ϕ_R from 0 to 0.2. In that case a ridge with identical strain incurs a 78% expansion in ridge width, and 38% inflation in keel depth relative to the ridge state represented in the ridge-wide thickness distribution, $g_R(h, 0)$. This problem can only be fixed by ensuring physical consistency of the ridge state used for form-drag with the Euler-Lagrange equation (13) that accounts for evolution of ϕ_R. We will derive new mass and momentum evolution equations to achieve this.

0.5.3. Shear and Slope

There is little precedent for the mathematical representation of shear ridges in models, although *Flato and Hibler* [1995] parameterized strike-slip floe motion by increasing frictional energy loss under large-scale shearing. No taxonomic separation of pressure and shear ridges exists, but sea ice topography formed under low and high θ_R values is distinguishable by sail steepness and rubble content [*Weeks*, 2010]. Whereas pressure ridges are typically composed of well-cut ice blocks, ridged rubble generated under horizontal shear takes a mangled appearance. An example of this difference may be seen for 'pressure' and 'shear' ridges in Figures 1a and 1b, respectively. The shear ridge is steeper than the ridge created primarily under compressional stress, common of sheared kinematic features extending many kilometers across the pack [*Weeks*, 2010]. *Roberts* [2018a] provides short audiovisual footage of ridging under predominant compressional and shearing conditions, and demonstrates the associated differences in ridge morphology. Within our coarse-grained model, the exact nature of rubble, mangled or not, is a fine-grained detail unrepresented by bulk porosity. An increase in ridge steepness as $\theta_R \to 90°$ naturally occurs as part of the coarse-grained description, similar to actual ridges.

This shear-slope relationship is demonstrated in Figure 9 where the compressional angle of repose, α_R, and deformational angle, θ_R, have no impact on sail height nor keel depth. Instead, they only affect the width of the ridge, L_K. The deformational state in Figure 9a is the same as in Figure 5a and represents a pressure ridge ($\theta_R = 180°$). By intoducing shear in Figure 9b ($\theta_R = 125°$), the angle of keel repose increases from 22° to 35.2° via the relation $\alpha_K = \operatorname{arccot}(\cos(\pi - \theta_R)\cot\alpha_R)$, even as the slope oriented along the compressional $\hat{x}$-axis (α_R) is unchanged. The plan-view in Figures 4 helps explain the

geometry associated with strike-slip deformation, in which the red-arrowed lines mark the pressure- and shear-ridge transects in Figure 9. At all times, the compressional breadth of the ridge $\hat{L}_K$ *along the* $\hat{x}$*-axis* remains the same, even though the cross-sectional width, L_K, decreases with increasing shear so that the keel and sail become steeper. Even when θ_R is held constant and the compressional angle of repose α_R is changed, neither H_K nor H_S are affected. This is a natural consequence of isostasy, and means that α_K has no impact on the ridge-wide bivariate thickness distribution, $g_R(h, \phi_R)$, as demonstrated in appendix B. However, shear does affect $g(h, \phi_R)$ when applying this morphology to the entire pack.

Coarse-Grained Ridge Mechanics

In this section, we derive Ψ from first principles for individual ridges using the polygonal morphology established in section 0.3. To achieve this, we quantify each term in the simplified Euler-Lagrange equation in (13) for a single ridge. Derivations of the associated kinetic energy and potential energy densities, $\mathcal{T}$ and $\mathcal{V}$ respectively, are relatively easy and are presented in appendix C. The friction model defining the non-conservative compressive stress $\boldsymbol{\mathcal{Q}}_{\hat{x}}$ is less straightforward, and so it is important to clearly lay out the assumptions, advantages and limitations of our representation of dissipative energy loss. Using the Euler-Lagrange equation, we constrain a ridge's state space in terms of ϵ_{R_I}, ϕ_R, and α_R using variational methods. This results in a continuity equation for macroporous ice that is extensible to a redistribution function over an area of the pack with many forming ridges. Snow cover is omitted from the proceeding derivations because its subtle morphological influence is peripheral to our main results (see supporting material). We need only derive

terms for symmetric ridges, because asymmetric ridges are derivable from the defined half-ridge morphology.

0.6. Coulombic Friction Model

We require the term $\boldsymbol{\mathcal{Q}}_{\hat{x}} = \partial_{\hat{x}}\sigma_{\hat{x}} - \partial_{\hat{x}}\mathcal{V}$ to be computationally efficient and sufficiently accurate to solve equation (13) in ESMs. There are several established constitutive relations that express the local ridge stress tensor, $\boldsymbol{\sigma}_R$, in terms of the horizontal strain tensor, $\boldsymbol{\epsilon}_R$, including those reviewed by *Timco et al.* [2000] and *Heinonen* [2004]. The most appropriate for our task assumes that a rubble pile fails as a Coulombic granular material, with a bulk critical angle of friction ψ_R through the compressional $(\hat{x}, \hat{z})$ plane, as demonstrated in Figure 10. This is the model of *Mellor* [1980], which has subsequently been used in several ridging studies [e.g. *Hopkins et al.*, 1991; *Kuuliala et al.*, 2017]. Although we term this a friction model for brevity, we are using the approximation to represent both generation and grinding of rubble.

0.6.1. Rankine State

Orientation of our polygonal ridges means that the local three-dimensional Cauchy stress tensor can be diagonalized into principal horizontal compressive and shear components, and one vertical component, following *Mellor* [1986] and *Hopkins et al.* [1991]. By definition, there is no horizontal shear on the $(\hat{x}, \hat{z})$ plane, so that a ridge's stress field can be further reduced to a two-dimensional, coarse-grained tensor with respective compressive and vertical stress components, $\sigma_{R_{\hat{x}}}$ and $\sigma_{R_{\hat{z}}}$, integrated over the entire ridge:

$$\boldsymbol{\sigma}_R = \begin{bmatrix} \sigma_{R_{\hat{x}}} & 0 \\ 0 & \sigma_{R_{\hat{z}}} \end{bmatrix} \tag{14}$$

$\sigma_{R_{\hat{x}}}$ and $\sigma_{R_{\hat{z}}}$ are related by assuming that each ridge acquires a Rankine state of passive failure, with an associated coefficient of passive stress:

$$K_p = \frac{\sigma_{R_{\hat{x}}}}{\sigma_{R_{\hat{z}}}} = \left(\frac{1+\sin\psi_R}{1-\sin\psi_R}\right). \tag{15}$$

In the Rankine passive state, gravity and shear resist the vertically-integrated compressive stress $\sigma_{R_{\hat{x}}}$, which is minimized so that the structure reaches an equilibrium [*Barnes*, 2016]. We assume ice within the ridge is cohesionless. We also assume there is no friction down the leading ridge edges nor the ridge line (Fig. 10). These assumptions make ψ_R constant within each ridge half, as demonstrated for retaining walls by *Lambe and Whitman* [1969].

Whereas *Hopkins et al.* [1991] assumed ψ_R and α_R were equal, Rankine theory does not permit this premise within our polygonal configuration. Instead, a necessary condition of (15) is that a critical failure plane extends from the sea surface at the ridge's leading edges diagonally down to the keel crest, as seen in Figure 10:

$$\tan\psi_R = \frac{H_K}{H_K - h_{F_d}} \tan\alpha_R. \tag{16}$$

Equation (16) conjoins the passive failure zones resulting from level ice traction against the ridge's submerged edge, and from brash pushing against a keel half from the opposite side of the rubble pile. Following *Mellor* [1980], it is capped at the sea surface by the weight of the sail. If the slip planes were less inclined, the keel's passive failure zone would extend beyond the defined ridge boundary. If the slip planes were more inclined, an equilibrium would not exist. The failure planes are continuous, and so ψ_R is the same in freeboard ice as in the submerged material (Fig. 10).

The mean vertical stress $\sigma_{R_{\hat{z}}}$ within a half-ridge is the weight of its floating ice, minus the weight of the associated displaced water, integrated across its width $\hat{x} \in [0, \hat{L}_K/2]$.

Applying (15) provides a term for the *Mellor* [1980] resistive stress, which in our case equates to $\sigma_{R_{\hat{x}}}$:

$$\sigma_{R_{\hat{x}}} = K_p \int_0^{\hat{L}_K/2} \left(\int_{-h_d}^{h_f} \rho\, \hat{g}(1-\phi_R)\, d\hat{z} - \int_{-h_d}^{0} \rho_w\, \hat{g}(1-\phi_R)\, d\hat{z} \right) d\hat{x}. \tag{17}$$

Combining equations (13) to (16), noting that the term on the right hand side of (17) is a multiple of potential energy density $\mathcal{V}$ in appendix C (25), and focusing on the ridge-scale where $\sigma_{\hat{x}} = \sigma_{R_{\hat{x}}}$ and $\sigma_{R_{\hat{x}}} = K_p\, \sigma_{R_{\hat{z}}}$, a mature ridge in a static state is governed by the functional:

$$0 = \delta \int_{t_\mathrm{i}}^{t_\mathrm{f}} \int_A K_p\, \mathcal{V}\, dA\, dt \tag{18}$$

Lagrange's δ term shifts to the front of the integral, creating the functional, because the variation $\delta\hat{x}$ is only tested for a single term in the integrand. Equation (18) applies individually along any path $\hat{x}$ of ridging ice, but without further physical insight, it may only be assumed to be true if the ridge is in a static state (i.e. $\mathcal{T} = 0$). Further insight comes from our source of energy loss, $\boldsymbol{\mathcal{Q}}_{\hat{\boldsymbol{x}}}$.

0.6.2. Non-Conservative Force

Applying equations (13) to our coarse-grained rubble pile, and combining it with (25) and (17) produces an equality for the non-conservative compressional force per unit ridge area $\boldsymbol{\mathcal{Q}}_{\hat{\boldsymbol{x}}}$ that applies throughout ridge evolution ($\mathcal{T} \geq 0$):

$$\boldsymbol{\mathcal{Q}}_{\hat{\boldsymbol{x}}} = \partial_{\hat{x}} \left(\sigma_{R_{\hat{x}}} - \mathcal{V} \right) = \partial_{\hat{x}} \left[(K_p - 1)\mathcal{V} \right] \tag{19}$$

Equation (19) is made possible by the fact that $m\, d\dot{\hat{x}}/dt = d(\partial_{\dot{\hat{x}}}\mathcal{T})/dt$ in (13) and the result $\sigma_{R_{\hat{x}}} = K_p\mathcal{V}$ that emerges from our chosen friction model. The non-conservative frictional force is thus independent of time, and $\boldsymbol{\mathcal{Q}}_{\hat{\boldsymbol{x}}}$ is determined solely from a conservative potential. By construction, K_p is a ratio of lengths, independent of velocity, and

is constant throughout each ridge half. Because of this, and since $\boldsymbol{\mathcal{Q}}_{\hat{\boldsymbol{x}}}$ can be expressed solely as a multiple of $\mathcal{V}$, we can eliminate non-conservative terms from a Euler-Lagrange equation for sea ice ridging, and therefore (18) ensures stationarity of the system along individual paths $\hat{x}$ for all $\mathcal{T} \geq 0$ [*Galley*, 2012; *Galley et al.*, 2014]. That is, we can now apply a least action principle to ridging because we have defined a *monogenic* system from which we may gain insight into constraints on $g_R(h, \phi_R)$.

0.7. Monogenic Ridging Equations

Just as *Rothrock* [1975] defined frictional loss purely in terms of potential energy, so have we. But within our variational construct and choice of friction model, we can take Rothrock's method one step further, with important consequences. We can use equation (18) to constrain porosity (ϕ_R) and the angle of repose (α_R) for given tensile strain (ϵ_{R_I}) and boundary conditions h_F and θ_R. This step is crucial for later calculating Ψ over broader regions of the pack (section 0.7.4).

0.7.1. The Euler-Lagrange Equation

The functional in (18) may be rewritten in terms of $\sigma_{R\hat{x}} = \sigma_{R\hat{x}}(\epsilon_{R_I}, \phi_R, \alpha_R)$ for the boundary condition h_F, leading to the alternate form:

$$0 = \int_{t_\mathrm{i}}^{t_\mathrm{f}} \int_A \left(\frac{\partial \sigma_{R\hat{x}}}{\partial \epsilon_{R_I}} \frac{\partial \epsilon_{R_I}}{\partial \hat{x}} + \frac{\partial \sigma_{R\hat{x}}}{\partial \phi_R} \frac{\partial \phi_R}{\partial \hat{x}} + \frac{\partial \sigma_{R\hat{x}}}{\partial \alpha_R} \frac{\partial \alpha_R}{\partial \hat{x}} \right) \delta \hat{x} \, dA \, dt \tag{20}$$

Equation (20) reduces to $\delta \sigma_{R\hat{x}} = 0$, and a necessary and sufficient condition that stationarity exist for $\sigma_{R\hat{x}}$ within the state space ϵ_{R_I}, ϕ_R and α_R is that each term within the parenthesis vanishes at the stationary point [*Lanczos*, 1970]. A further constraint is imposed by our chosen friction model in that the system must remain in the Rankine equilibrium state described in section 0.6.1. This means that for all possible values of ϵ_{R_I} and ϕ_R, the

last term in parenthesis always vanishes by itself. Appendix D demonstrates that there is a non-trivial solution for $\partial_{\alpha_R}\sigma_{R\hat{x}} = 0$ so that the right hand product inside the parenthesis in (20) vanishes for an angle of repose at the extremum $\alpha_R{=}\hat{\alpha}_R(\epsilon_{R_I}, \phi_R)$. Therefore, ridge states must lie within the potential energy density $\mathcal{V}_R = \mathcal{V}(\epsilon_{R_I}, \phi_R, \hat{\alpha}_R, h_F)$. A corollary of $\partial_{\alpha_R}\sigma_{R\hat{x}} = 0$ is that the coefficient of passive failure becomes constant and takes the value $K_p = 3$ (appendix D). Remarkably, this is within the range $2.4 \leq K_p \leq 4.6$ estimated from discrete element ridge simulations by *Hopkins et al.* [1991].

Figure 11 illustrates two surfaces of $\mathcal{V}_R(\epsilon_{R_I}, \phi_R, \hat{\alpha}_R, h_F)$ representing h_F=0.5 and 2.0 m, color shaded to indicate the $\hat{\alpha}_R$ solution of $\partial_{\alpha_R}\sigma_{R\hat{x}} = 0$. As with real ridging, the angle of repose begins at zero when there is no strain or porosity, and it increases with either or both $-\epsilon_{R_I}$ and ϕ_R. In our solution, $\hat{\alpha}_R$ approaches a limit of 30° at maximum porosity and compressional strain, amounting to a keel slope zenith of $\alpha_K{=}\arctan[\sec(\pi{-}\theta_R)\tan(\pi/6)]$. Each point in $\mathcal{V}_R$ represents a unique ridge state as determined by the keel depth, H_K, sail height H_S, compressional width, $\hat{L}_K$, porosity, ϕ_R, compressional angle of repose, α_R, and parent thickness, h_F. Evidence of the verity of our coarse-grained approximation exists in the close alignment of ridge states for maximum sail height $H_{S_{\max}} = 5.24\sqrt{h_F}$, and keel depth $H_{K_{\max}} = 16\sqrt{h_{F_d}}$, using empirical estimates from observations by *Tucker et al.* [1984] and *Melling and Riedel* [1996], respectively (Fig. 11). Were the $H_{S_{\max}}$ and $H_{K_{\max}}$ tracers not closely aligned with one-another on $\mathcal{V}_R$ surfaces, it would indicate that the coarse-grained morphology and variational mechanics did not mimic the observed ridge state space of mature ridges. While it seems that both the maximum sail height and keel depth tracers are also aligned with $\hat{\alpha}_R$ contours in Figure 11, this apparent correlation is not present in the case of snow loading (not presented

here). With or without snow, $H_{K_{\max}}$ lies in close proximity to $H_{S_{\max}}$ within $\mathcal{V}_R$. As a consequence of K_p remaining constant, our Euler-Lagrange equation is:

$$0 = \tfrac{1}{3}\frac{d}{dt}\frac{\partial \mathcal{T}}{\partial \dot{\hat{x}}} - \frac{\partial \mathcal{V}_R}{\partial \hat{x}} \tag{21}$$

Equation (21) is the expression of (13) after applying $\boldsymbol{\mathcal{Q}}_{\hat{x}}$ in (19) using $\sigma_{R_{\hat{x}}} = K_p\,\mathcal{V}$ from (17) and $K_p = 3$ from (32). The important point of (21) is that it isolates conversions between kinetic energy and (conservative) potential energy.

0.7.2. Dilation of Potential Energy Density

Applying the relations leading to (21), the variational principle in (20) now takes the familiar form of a conservative system, expressed in terms of a potential gradient:

$$0 = \int_{t_\mathrm{i}}^{t_\mathrm{f}} \int_A \left(\frac{\partial \mathcal{V}_R}{\partial \epsilon_{R_I}}, \frac{\partial \mathcal{V}_R}{\partial \phi_R}\right) \cdot \left(\frac{\partial \epsilon_{R_I}}{\partial \hat{x}}, \frac{\partial \phi_R}{\partial \hat{x}}\right) \delta\hat{x}\; dA\; dt \tag{22}$$

By variational calculus, the scalar product of the vector fields in parentheses in (22) is zero and the fields are orthogonal. The first vector field is a potential density gradient we define as the *Dilation Field*, $\mathbf{đ} = \mathbf{đ}(đ_1, đ_2)$:

$$\mathbf{đ} = \nabla_R \mathcal{V}_R = \left(\frac{\partial \mathcal{V}_R}{\partial \epsilon_{R_I}}, \frac{\partial \mathcal{V}_R}{\partial \phi_R}\right) \tag{23}$$

where $\nabla_R = (\partial_{\epsilon_{R_I}}, \partial_{\phi_R})$. The Dilation Field is the rate of change of potential energy with respect to strain and porosity in the space $\boldsymbol{\zeta} = (\epsilon_{R_I}, \phi_R)$. $\mathbf{đ}$ describes the energetics associated with the decrease in area-averaged density of ridging material. As cavities open up within ridges, the bulk density of the ridge differs from the ice density ρ of intact floes and rubble blocks, which impacts the rate of increase of potential energy density. $\mathbf{đ}$ permits us to account for ice density changes in the sea ice momentum equation due to ridging, which is a requirement for that equation to become scale-aware when accounting for vertical deformation over a broad area of the pack in section 0.7.4. The second vector

field in (22) is the covariant derivative, $\boldsymbol{\zeta}_{\hat{x}}$, representing the change in ϵ_{R_I} and ϕ_R with respect to the compressional axis:

$$\boldsymbol{\zeta}_{\hat{x}} = \frac{\partial \boldsymbol{\zeta}}{\partial \hat{x}} = \left(\frac{\partial \epsilon_{R_I}}{\partial \hat{x}}, \frac{\partial \phi_R}{\partial \hat{x}} \right) \tag{24}$$

Both $\mathbf{đ}$ and $\boldsymbol{\zeta}$ are important for defining virtual work density, $\delta\mathcal{W}$, for which we are afforded the simplification $K_p\,\mathbf{đ} = \nabla_R\,\sigma_{R\hat{x}}$ because K_p is constant.

The principle of virtual work equates ridging work inside the (ϵ_{R_I}, ϕ_R) domain with the work at its perimeter, $C_{\hat{x}}$, using the divergence theorem:

$$\delta\mathcal{W} = \int_{\phi_R} \int_{\epsilon_{R_I}} \left(\frac{\partial \mathbb{P}}{\partial \epsilon_{R_I}} + \frac{\partial \mathbb{Q}}{\partial \phi_R} \right) d\epsilon_{R_I}\, d\phi_R - \oint_{C_{\hat{x}}} (\mathbb{P}, \mathbb{Q}) \cdot \left(\frac{\partial \phi_R}{\partial \hat{x}}, -\frac{\partial \epsilon_{R_I}}{\partial \hat{x}} \right) d\hat{x} \tag{25}$$

where

$$\mathbb{P} = \frac{\partial \sigma_{R\hat{x}}}{\partial \epsilon_{R_I}}\,\delta\hat{x}, \qquad \mathbb{Q} = \frac{\partial \sigma_{R\hat{x}}}{\partial \phi_R}\,\delta\hat{x}.$$

The vector field $(\mathbb{P}, \mathbb{Q})$ is the force applied at the boundary of the domain $\epsilon_{R_I} \in (-1, 0]$ and $\phi_R \in [0, 1)$ under the variation $\delta\hat{x}$, and the vector $(\partial_{\hat{x}}\phi_R, -\partial_{\hat{x}}\epsilon_{R_I})$ is normal to $\boldsymbol{\zeta}_{\hat{x}}$ and points outward from the perimeter. Given $\epsilon_{R_I} = \epsilon_{R_I}(\hat{x})$ and $\phi_R = \phi_R(\hat{x})$, the variation of $\boldsymbol{\zeta}$ is

$$\delta\boldsymbol{\zeta} = (\delta\epsilon_{R_I}, \delta\phi_R) = \left(\frac{\partial \epsilon_{R_I}}{\partial \hat{x}}\,\delta\hat{x}, \frac{\partial \phi_R}{\partial \hat{x}}\,\delta\hat{x} \right). \tag{26}$$

Dividing (25) by K_p, then applying Hamilton's Principle for our conservative system defined in (21) gives:

$$0 = \int_{\phi_R} \int_{\epsilon_{R_I}} \big(\nabla_R \cdot \mathbf{đ}\big)\delta\hat{x}\, d\epsilon_{R_I}\, d\phi_R - \oint_{C_{\hat{x}}} |\mathbf{đ} \times \delta\boldsymbol{\zeta}|\, d\hat{x}. \tag{27}$$

We can now make a key physical insight because we have restated our initial condition problem as a boundary condition problem. There is an initial condition of zero strain and macroporosity, which in (27) equates to the boundary condition $\boldsymbol{\zeta}_0 = (0, 0)$, and that

means that $|\delta\boldsymbol{\zeta}|=0$; there is no variation at the boundary. Consequently, the right-hand term in (27) vanishes, and we are left with the integral:

$$0 = \int_{\phi_R} \int_{\epsilon_{R_I}} \left(\nabla_R \cdot \mathbf{đ}\right) \delta\hat{x} \, d\epsilon_{R_I} \, d\phi_R. \tag{28}$$

This is an analogous variational case to the sea ice momentum equation example in (3), but in this case, we are left with the continuity equation for coarse-grained ridging under the first-order variation $\delta\hat{x}$:

$$\nabla_R \cdot \mathbf{đ} = 0 \tag{29}$$

In practical terms, we have used the divergence theorem to eliminate the local coordinate $\hat{x}$ from our equations, thereby revealing the energetic consequence of macroporosity for our chosen friction model, regardless of the local ridge coordinate system.

Equation (29) is our core governing equation to be applied within ESMs. Since $\mathcal{V}_R$ is a scalar, then $\nabla_R \times (\nabla_R \mathcal{V}_R) = 0$, and $\mathbf{đ}$ must be irrotational ($\nabla_R \times \mathbf{đ} = 0$). Laplace's equation must then apply to both $\mathcal{V}_R$ and a corresponding stream function Υ_R, whereby ${\nabla_R}^2 \mathcal{V}_R = 0$ and ${\nabla_R}^2 \Upsilon_R = 0$, and:

$$đ_1 = \frac{\partial \mathcal{V}_R}{\partial \epsilon_{R_I}} = \frac{\partial \Upsilon_R}{\partial \phi_R}, \qquad đ_2 = \frac{\partial \mathcal{V}_R}{\partial \phi_R} = -\frac{\partial \Upsilon_R}{\partial \epsilon_{R_I}} \tag{30}$$

This means that we can predict ϕ_R and α_R based purely on ϵ_{R_I} using the streamline $\boldsymbol{\zeta} = \hat{\boldsymbol{\zeta}}(\epsilon_{R_I}, \phi_R, \hat{\alpha}_R)$ that passes through the initial condition $\boldsymbol{\zeta}_0$, annotated as red state-space trajectories in $\mathcal{V}_R$ in Figure 11, and defined by:

$$\phi_R(\hat{\boldsymbol{x}}) = \int_0^{\epsilon_{R_I}(\hat{\boldsymbol{x}})} \frac{đ_2}{đ_1} \, d\epsilon_{R_I} \tag{31}$$

Equation (31) represents ridging as an initial value problem because the ridge-wide thickness distribution $g_R(h, \phi_R)$ can now be predicted purely in terms of initial conditions $\boldsymbol{\zeta}_0$

and h_F, as well as strain at a later time. Conversely, equation (31) may be inverted to determine strain from porosity and the initial condition. Either way, the state space trajectory $\hat{\boldsymbol{\zeta}}$ is only dependent upon initial conditions rather than boundary conditions in time, thus addressing a limitation of existing ridging parameterizations discussed in section 0.2.

0.7.3. State Space Trajectory $\hat{\boldsymbol{\zeta}}$

It is important to understand what the state space trajectory $\hat{\boldsymbol{\zeta}}$ means in relation to the potential energy density $\mathcal{V}_R$. To aid understanding, we have re-rendered the h_F=2 m $\mathcal{V}_R$ surface from Figure 11 and presented it in plan-view in Figure 12, now color shaded for values of $\mathcal{V}_R$ rather than for $\hat{\alpha}_R$ as in Figure 11. Streamlines of the dilation field $\mathbf{đ}$ are superimposed on Figure 12, which are perpendicular to the $\mathcal{V}_R$ contours. This must be the case, because $\mathbf{đ}$ is by definition the gradient in (conservative) potential energy density with respect to ϵ_{R_I} and ϕ_R. It is easy to see from this figure that $\hat{\boldsymbol{\zeta}}$ is the unique streamline that passes through initial condition $\boldsymbol{\zeta}_0 = (0, 0)$, and thus describes evolution of the conservative part of the system.

Combining $\nabla_R \cdot \mathbf{đ} = 0$ with the initial condition $\boldsymbol{\zeta}_0$ presents a classic Dirichlet problem, and allows us to formalize the constraint for which ridging is stationary:

$$0 = \delta \int_{\phi_R} \int_{\epsilon_{R_I}} \left(\nabla_R \mathbf{đ} \cdot \nabla_R \mathbf{đ} \right) d\epsilon_{R_I} \, d\phi_R \tag{32}$$

The functional in (32) stems from the Laplacian ${\nabla_R}^2 \mathcal{V}_R = 0$. Its generic proof is common in variational texts [e.g. *Wan*, 1995] and is omitted here for brevity. The variational principle in (32) is naturally enacted by applying the continuity equation in (29) in conjunction with predicting porosity $\phi_R = \phi_R(\epsilon_{R_I})$ and ridge shape $\alpha_R = \hat{\alpha}_R(\epsilon_{R_I}, \phi_R)$ using $\hat{\boldsymbol{\zeta}}(\epsilon_{R_I}, \phi_R)$

determined from equation (31). Mass conservation laws naturally precipitate from these equations, including the redistribution function of an individual ridge.

0.7.4. Redistribution of Ice in an Individual Ridging Event

The continuity equation $\nabla_R \cdot \dot{\mathbf{d}} = 0$ permits the thickness distribution $a_R(h, \phi_R, \boldsymbol{x})$ of an individual coarse-grained ridge to be determined purely from the boundary conditions h_F and θ_R, as well as strain. $a_R(h, \phi_R, \boldsymbol{x})$ is the ridge-scale, bivariate analogue of the pack-scale distribution of deforming ice $a(h, \boldsymbol{x})$ in the ridging mode in (8). $a_R(h, \phi_R, \boldsymbol{x})$ includes the effect of macroporosity on sea ice thickness and is scaled against the thickness distribution $g_R(h, \phi_R, \boldsymbol{x})$ introduced in section 0.3 and derived in appendix A:

$$a_R(h, \phi_R, \epsilon_{R_I}, \boldsymbol{x}) = (1 + \epsilon_{R_I})\, g_R(h, \phi_R, \boldsymbol{x}) \tag{33}$$

Whereas $g_R(h, \phi_R, \boldsymbol{x})$ is normalized over the deforming width of a ridge, $a_R(h, \phi_R, \epsilon_{R_I}, \boldsymbol{x})$ is normalized over the material area $A(\boldsymbol{x})$, which is non-deforming. Since the area of deforming ice is reduced by the ratio of ridge width to its undeformed width, including in the presence of shear, the factor $L_K/L_F = (1 + \epsilon_{R_I})$ appears in (33). Given that *all ice* is deforming in a ridge, the material derivative of $a_R(h, \phi_R, \boldsymbol{x})$ defines ridge redistribution in equation (2), but just for one ridge, where $g(h, \phi_R) = g_R(h, \phi_R)$:

$$\Psi = \frac{d\, a_R}{dt} \tag{34}$$

To obtain an expression for $a_R(h, \phi_R, \boldsymbol{x})$ purely in terms of variables ϵ_{R_I}, ϕ_R, and h_F, ρ_w, and ρ, we substitute for L_K, L_S and α_K in the $g_R(h, \phi_R, \boldsymbol{x})$ step function (19) using equations (1) to (4), (9), (13) to (16) and (33). Using these steps, we can efficiently solve for (34) from changes to the distribution $g(h_F, \phi_F)$ with initial parent-sheet macroporosity

ϕ_F using the integral transform:

$$a_R(h, \phi_R, \epsilon_{R_I}) = \int_0^{\infty} \int_0^{1} g(h_F, \phi_F)\, \gamma(h_F, h - h_F, \phi - \phi_F, \epsilon_{R_I})\, d\phi_F\, dh_F \tag{35}$$

since $\epsilon_{R_I} = \int_{t_i}^{t_f} \dot{\epsilon}_{R_I}\, dt$ for a given strain rate $\dot{\epsilon}_{R_I}$. γ is an impulse response function composed of two step functions,

$$\gamma(h_F, h, \phi, \epsilon_{R_I}) = \Pi^-(h_F, h, \phi, \epsilon_{R_I}) + \Pi^+(h_F, h, \phi, \epsilon_{R_I}). \tag{36}$$

where Π^- and Π^+ derive from the successive $g_R(h, \phi_R, \boldsymbol{x})$ steps introduced in section 0.3 and seen in Figure 7, for which the analytic form in terms of ϵ_{R_I}, ϕ_R, and h_F is:

$$\Pi^{\pm} = \frac{1}{2h_F} \frac{\rho_w}{\rho} (1 + \epsilon_{R_I})\, \Gamma(\epsilon_{R_I})\, \hat{\delta}(\phi - \phi_R) \left[H\left(\Xi^{\pm}\right) + H\left(\Xi^{\pm} - 1\right) \right] \tag{37}$$

for the Heaviside function, H, Dirac delta function, $\hat{\delta}$, deformation ratio,

$$\Gamma(\epsilon_{R_I}) = \tfrac{1}{2} \frac{(1 + \epsilon_{R_I})(1 + \phi_R)}{(\phi_R + \epsilon_{R_I}\, \phi_R - \epsilon_{R_I})}, \tag{38}$$

and operator

$$\Xi^{\pm} = \frac{h}{h_F} \frac{\rho_w\, \Gamma(\epsilon_{R_I})}{\rho \pm \sqrt{\Delta\rho\, \rho}}.$$

The continuity equation $\nabla_R \cdot \mathbf{đ} = 0$ ensures that because we know ridge strain ϵ_{R_I}, we also know the ridge porosity ϕ_R in $\Pi^{\pm}(h_F, h, \phi, \epsilon_{R_I})$ and $\Gamma(\epsilon_{R_I})$ using equation (31), and the $\pm$ superscript indicates the sign in the denominators of $\Xi^{\pm}$.

Equation 35 efficiently solves for Ψ using a fast fourier transform, and we demonstrate a simple example of its application in Figure 13. The $h_F = 2$ m parent ice sheet in Figure 11 has an initial local distribution $g(h, \phi_R) = \hat{\delta}(h - h_F, \phi)$, shown as a Dirac delta function in Figure 13. This corresponds to the initial condition of its $\hat{\boldsymbol{\zeta}}$ trajectory which is marked with a small violet cross in Figure 11. As strain increases, the distribution of the individual ridge, $a_R(h, \phi_R, \epsilon_{R_I}, \boldsymbol{x})$, represents a smaller and smaller area relative to the

region initially covered by the parent ice, and the ridge becomes steeper, more porous, and thicker, as seen in the ever 'flattening' step functions for $\epsilon_{R_I} = -0.2$, -0.4 and -0.6 (Fig. 13). These respective distributions trace progression of the ridge through $\mathcal{V}_R$ in Figure 11, as marked. At all times, the mass density of deforming ice, m, is unchanged, as given by

$$m = \rho \int_0^{\infty} \int_0^{1} a_R(h, \phi_R, \epsilon_{R_I}, \boldsymbol{x}) \, (1 - \phi) \, h \, d\phi \, dh \tag{39}$$

and mass is conserved.

Using $a_R(h, \phi_R, \epsilon_{R_I}, \boldsymbol{x})$ derived here for a single coarse-grained ridge, we are ready to take the final step by applying it to redistribution over fields of ridges. We combine this with the Euler-Lagrange equation in section 0.7.1 to determine compressive stress P of the pack as a whole. We will demonstrate that redistribution can be approximated as a series of step functions, built upon the impulse response function $\gamma = \Pi^- + \Pi^+$ of a single ridge.

Variational Ridging for Earth System Models

By ensuring stationarity, an important relationship emerges in the motion equation of sea ice beyond the scale of just one ridge. That relationship determines the probability of finding ridges of different shapes and sizes in the pack, and therein lies the main applicability of variational ridging to Earth system modeling. In this section, we demonstrate the statistical consequence of stationarity in ridging using our chosen Coulombic friction model, and we derive momentum and mass balance equations for the pack as a whole.

0.8. Redistribution of a homogenous sea ice field

Ridge frequency statistics emerge from the stationary principle in (20) when considering deformation over a sea ice field with an initially uniform thickness h_F, no macroporosity,

and 100% sea ice concentration. From equations (18) and (21), the principle of virtual work for a ridge is the functional:

$$0 = \delta \iint_A \mathcal{V}_R \, dA \tag{40}$$

We may break down the integration over A into the orthogonal $\hat{x}$ and $\hat{y}$ coordinates (section 0.3), as illustrated in Figure 4 for the total length of ridged ice with a particular strain and initial thickness, $\hat{W}$. Stationarity is then determined by the functional:

$$0 = \delta \int_0^{\hat{W}} \int_0^{\hat{L}_K} \mathcal{V}_R \, d\hat{x} \, d\hat{y} \tag{41}$$

Owing to the fact that $\mathcal{V}_R$ and $\hat{L}_K$ have been coarse-grained for a given ϵ_{R_I} and h_F, the area integral in (41) simplifies to the variation:

$$\delta\big(\hat{W}(\epsilon_{R_I}, h_F)\ \hat{L}_K(\epsilon_{R_I}, h_F)\ \mathcal{V}_R(\epsilon_{R_I}, h_F)\big) = 0. \tag{42}$$

Hence, large ridges with considerable keel depth and cross-sectional width $\hat{L}_K$ must occur infrequently; their total length over A, quantified in (42) by $\hat{W}$, shall be small relative to an abundance of small ridges, whose total length along many floe edges will be large. $\hat{W}$ therefore serves as a proportionality constant over A, and

$$U_R = \hat{W}(\epsilon_{R_I}, h_F)\ \hat{L}_K(\epsilon_{R_I}, h_F)\ \mathcal{V}_R(\epsilon_{R_I}, h_F) \tag{43}$$

is the total potential energy that is identical for all ridged areas regardless of compressional strain and initial thickness.

$\hat{W}$ is the *apparent ridge length* along the compressional axis. Due to the effect of shear between individual floes, the actual ridge length seen in aerial images of the pack for a given ridge shape is $W_R = \hat{W}\sec(\pi - \theta_R)$ (Fig. 4). The consequence of this is that shear ridges (e.g. Figure 1b) can extend a long way across the pack and between floes

relative to the equivalent length of pressure ridges (e.g. Figure 1a). This agrees with the observations of long shear ridges noted by *Weeks* [2010]. However, we have purposely removed θ_R from explicit mention in these equations, because the mathematical notation becomes cumbersome and may cloud understanding of the results. By using $\hat{W}$ and $\hat{L}_R$ hencefourth, the possible presence of shear remains implicit and its significance is not lost.

Equation (42) provides the relationship between ridges of different shapes and sizes that does not need empiricisms for us to progress to its application to the large scale. The fraction of energy per unit $\hat{W}(\epsilon_{R_I}, h_F)$ over all possible strains ϵ_{R_I} is given by

$$\Lambda(\epsilon_{R_I}, h_F) = \frac{\int_{-1}^{0} \hat{L}_K(\epsilon_{R_I}, h_F)\ \mathcal{V}_R(\epsilon_{R_I}, h_F)\ d\epsilon_{R_I}}{\hat{L}_K(\epsilon_{R_I}, h_F)\ \mathcal{V}_R(\epsilon_{R_I}, h_F)} \tag{44}$$

The integral appears in the numerator because $\hat{W}$ is inversely proportional to $\hat{L}_K\ \mathcal{V}_R$. Equation (44) in turn gives the probability density, $b_R(\epsilon_{R_I}, h_F)$, of encountering a ridge of a certain shape and size that may be formed from an undeformed ice thickness, h_F, which exists in our bivariate thickness distribution as $g(h_F, \phi_R = 0)$:

$$b_R(\epsilon_{R_I}, h_F) = \frac{g(h_F, 0)\ \Lambda(\epsilon_{R_I}, h_F)}{\int_{-1}^{0} g(h_F, 0)\ \Lambda(\epsilon_{R_I}, h_F)\ d\epsilon_{R_I}} \tag{45}$$

The result codified in (45) means that over an area A of the pack with multiple ridges, Newton's second law applies for an initial thickness h_F if ridges are spatial separated at a distance dictated by their compressional strain. To demonstrate why this is the case, we make use of information in Figures 14 and 15 from our coarse-grained model. Figure 14 presents the diagram-of-state for stationary ridging action, which must sit on the $\hat{\boldsymbol{\zeta}}$-plane. Each point on this plane passes through the $\hat{\boldsymbol{\zeta}}$ trajectory of a given parent sheet with thickness h_F; the red $h_F = 0.5$ and 2.0 m trajectories in Figure 11 are annotated in

Figure 14 to illustrate this point. Every point on the $\hat{\boldsymbol{\zeta}}$-plane represents a unique ridge state with a singular $\mathcal{V}_R$, ϵ_{R_I}, ϕ_R, H_K, and $\hat{L}_K$ combination, and the local neighborhood of each point on a $\hat{\zeta}$-trajectory has a quantifiable probability of occurring relative to that of other points, illustrated for $b_R(\epsilon_{R_I}, 0.5\ m)$ and $b_R(\epsilon_{R_I}, 2.0\ m)$ in Figure 15. Ridge states that are likely to exceed observed limits, as suggested by *Tucker and Govoni* [1981], are indicated in Figure 14.

The relationship between $\hat{L}_K$ and $b(\epsilon_{R_I}, h_F)$ in Figure 15 is important because it imposes a constraint on the spatial occurrence of ridges in the pack. Moving up the red $\hat{\boldsymbol{\zeta}}$ trajectories in Figure 14, all of H_K (black contours), $\hat{L}_K$ (white contours) and $\mathcal{V}_R$ (shaded) increase exponentially relative to ϵ_{R_I}, although at slightly different rates relative to one-another. Consequently, there are close-fitting scaling relationships for probability of compressional width, $b_R \propto \hat{L}_K^D$, demonstrated for the latter in Figure 15, where D is a fitted scaling exponent. These relationships are notable due their consistency with scaling relations observed in horizontal sea ice divergence, shear and floe-size [e.g. *Paget et al.*, 2001; *Weiss*, 2003; *Marsan et al.*, 2004; *Stern and Lindsay*, 2009; *Perovich and Jones*, 2014]. The physical consequence of this quasi-scaling relationship is that an entire pack filled with tiny ridges over A at the limit $\epsilon_{R_I} \to 0_-$ is energetically identical to large, sparsely spaced ridges each with a high degree of compressive strain over the same region. The fractional area of ridged ice relative to level ice surrounding a ridge can therefore be articulated as:

$$c_{\text{ridged}}(\epsilon_{R_I}, h_F) = \frac{b_R(\epsilon_{R_I}, h_F)}{\lim\limits_{\epsilon_{R_I} \to 0_-} b_R(\epsilon_{R_I}, h_F)} \tag{46}$$

for a fixed initial and undeformed ice thickness h_F. For this reason large pressure ridges of the size seen in Figure 1a are seldom encountered in the pack, as was true of the region

surrounding that ridge during the Sea Ice Experiment - Dynamic Nature of the Arctic (SEDNA) field campaign [*Hutchings et al.*, 2008; *Doble et al.*, 2011; *Wadhams et al.*, 2011].

The statistical ridging relationship that emerges from (45) is not an empiricism, but instead a derived physical property. The power law suggested by that equation is not comparable with the log-normal spacing of ridges commonly measured over $A(x)$ [e.g. *Wadhams and Davis*, 1994; *Davis and Wadhams*, 1995; *Timco and Burden*, 1997; *Tan et al.*, 2012] because $b_R \propto \hat{L}_K^D$ gives the spatial occurrence of ridging at an instant, whereas observed log-normal ridge distributions are a hysteresis. Rather, one expects at an instant that the spatial distribution of ridging will observe a power law due to the concentration of deformation at the edge of floes, which themselves observe spatial scaling by way of the floes size distribution [e.g. *Paget et al.*, 2001; *Perovich and Jones*, 2014]. That such a distribution emerges from our chosen quantization gives credence to our coarse-grained methodolgy.

Matching the statistical outcomes of stationarity with observations is a delicate task, because deformations in $b_R(\epsilon_{R_I}, h_F)$ include, and are predominantly weighted toward, infinitesimal changes approaching the limit $\epsilon_{R_I} \to 0_-$. Small vertical displacements will escape detection by sonar, air- and space-borne altimeters, and will amount to uninteresting bumps in the cryoscape of an *in-situ* observer. Yet they are theoretically most likely, reflective of the fact that most sea ice does not deform or is minimally crushed when the pack is compressed. For the uniform field of sea ice 2.0 m thick in Figure 15, the mean porosity is $\bar{\phi}_R = 0.09$, and mean angle of repose $\bar{\alpha}_R = 10.4°$ within the prescribed limit of $-0.01 > \epsilon_{R_I} > -0.99$. However, if we apply a 5 m minimum cutoff to keel depth in (44), akin to the processing applied to submarine sonar by *Davis and Wadhams* [1995] and *Wad-*

hams et al. [2011], the mean values predicted by the coarse-grained model are $\bar{\phi}_R = 0.24$ and $\bar{\alpha}_R = 22.9°$, within close range of observational values cited in sections 1 and 0.3 ($0.2 - 0.3$ and $23.2°$, respectively). Further examples of this comparison are provided in Table 2. Note, however, that *Davis and Wadhams* [1995] could not resolve $\bar{\alpha}_R$, but only $\bar{\alpha}_K$, because measuring ridge shapes after they have formed does not indicate the amount of shear during their formation. Figure 6 presents our predicted porosity values (color shaded) for the sonar observation in pure compression ($\theta_R = 180°$) and with considerable shear ($\theta_R = 125°$). That figure illustrates that considerably different porosities, and hence α_R, could exist in each of the submarine-measured ridges when applying our method.

0.9. The Bivariate Redistribution Function

Combining derivation of the redistribution function $\Psi(h, \phi)$ for a single ridge in section 0.7.4 with the emergent probability of deformation $b_R(\epsilon_{R_I}, h_F)$ of a homogeneous ice cover in section 0.8, we can now derive the bivariate redistribution function for the pack as a whole. In the previous case of a homogeneous undeformed ice cover, there was no allowance nor need for varying the thickness and macroporosity of parent ice, nor for the presence of open water. To cater for heterogeneity reflected in $g(h, \phi_R)$, $b_R(\epsilon_{R_I}, h_F)$ in (45) becomes:

$$b(h_F, \phi_F, \epsilon_{R_I}) = \frac{H(\phi - \phi_F)\ \Lambda(h_F, \epsilon_{R_I})\ g(h_F, \phi_F)}{\int_0^\infty \int_0^1 \int_{-1}^0 \left(H(\phi - \phi_F)\ \Lambda(h_F, \epsilon_{R_I})\ g(h_F, \phi_F)\right) d\epsilon_{R_I}\ d\phi_F\ dh_F} \tag{47}$$

for an initial porosity ϕ_F, where the Heaviside function reflects the fact that $\Lambda(h_F, \epsilon_{R_I})$ need not describe ridging for less than the original porosity of deforming ice. The presence of open water is accommodated by evaluating $\Lambda(h_F, \epsilon_{R_I})$ at the limit $h_F \to 0$.

Using equation (47), the ridge-scale distribution $a_R(h, \phi_R, \epsilon_{R_I})$ at time t_f in (35) becomes:

$$a(h,\phi) = \int_0^\infty \int_0^1 \int_{-1}^0 \left(g(h_F,\phi_F)\, \gamma(h_F, h-h_F, \phi-\phi_F, \epsilon_{R_I})\, b(h-h_F, \phi-\phi_F, \epsilon_{R_I}) \right) d\epsilon_{R_I}\, d\phi_F\, dh_F \tag{48}$$

for the entire pack over A, thus providing a solution for redistribution in (2) as

$$\Psi = \frac{d\, a(h,\phi_R)}{dt} \tag{49}$$

where $a(h, \phi_R)$ is evaluated at time t_i in equation (48) as the initial distribution $g(h_F, \phi_F)$. The compressive stress, P, of the entire sea ice field is dictated by the fact that $\sigma_{\hat{x}} = K_p\, \mathcal{V}_R(h_F, \epsilon_{R_I})$ at the ridge scale in the final static state. Ridges are distributed according $b(h_F, \phi_F, \epsilon_{R_I})$, and therefore, P for a heterogenous pack is given by:

$$P = K_p \int_0^\infty \int_0^1 \int_{-1}^0 \left(\mathcal{V}_R(h_F, \epsilon_{R_I})\, b(h_F, \phi_F, \epsilon_{R_I}) \right) d\epsilon_{R_I}\, d\phi_F\, dh_F \tag{50}$$

0.10. $g(h)$ Integrated from $g(h, \phi_R)$

To conclude our theory, we return to the monovariate thickness distribution $g(h)$ first introduced by *Thorndike et al.* [1975]. In equation (1), we define $g(h)$ as an integrated form of $g(h, \phi_R)$. Using that equation, we can now demonstrate that $g(h)$ acquires qualitative properties akin to those expected from repeated ridging of the pack using the new redistribution function Ψ in (49). That is an initial value equation with boundary conditions h_F and ϵ_{R_I}, and we iteratively integrate the conservation equation (2) by calculating $a(h, \phi)$ for successive ridging events, renormalizing $g(h, \phi_R)$ at the end of each iteration to account for advection of converging ice entering the material area A. We neglect thermodynamics effects ($\Theta = 0$). Figure 16 demonstrates the evolution of an initially uniform

area of undeformed ice with thickness h_F=1 m under successive strain. At the end of the integration, a distribution is acquired with a tail qualitatively similar to that seen in observations of $g(h)$.

However, when judged against semilog axes (Fig. 16b), we note that the distribution $g(h)$ has not fully acquired a negative exponential tail typical of field measurements [e.g. *Wadhams et al.*, 1987; *Worby et al.*, 1996; *Haas et al.*, 2010]. If it had, the tail would appear as a straight line on the semilog axes. This suggests that thick ice is over-represented in the distribution, and points to missing physics, most probably in thermodynamics, where keels protruding deep into the oceanic boundary layer preferentially melt relative to shallow keels [*Davis and Wadhams*, 1995]. Therein lies a limitation of testing any redistribution function destined for deployment in ESMs without the complete spectrum of wind and ocean stress, and thermodynamic feedbacks. Therefore, in work to follow this paper, we will test the methods presented here with a model of ridge thermodynamics inside a fully coupled model. We will revisit the question as to whether the ridge mechanics, in conjunction with thermodynamics, can replicate measured statistical signals of ice thickness, and of freeboard.

For the mechanics focus of this paper, integration applied here can be performed with a MATLAB toolbox that accompanies this manuscript called *Ridgepack* [*Roberts*, 2018b] . *Ridgepack* provides a laboratory to help understand the practical implementation of theory presented in this paper as would be implemented in an ESM. Equations solved within the MATLAB package are referenced to specific equations in this paper, providing a practical tool for the implementation of the methods described. The toolbox may be used to generate most figures in this manuscript, including ridgegraphs, state-space

trajectories, and the $\hat{\zeta}$ plane. A Mathematica notebook is also available within *Ridgepack* to generate the step functions for individual ridges in Figure 13.

Discussion

We have used variational methods to derive the dynamics equations of sea ice in a way that accounts for the heterogeneity of ice thickness down to the scale of individual ridges. Whereas previous work has looked to physical analogues or empirical functions to determine the redistribution function Ψ, we have adopted the method of coarse-graining potential energy gain in terms of strain and the parent sheet thickness feeding individual ridges. The advantage of our method is that it reveals the statistical properties of ridges from monogenic equations we have derived to describe them. We have adopted a relatively simple Coulombic approximation of ridge mechanics to estimate $\boldsymbol{\mathcal{Q}}$ in terms of the conservative potential density $\mathcal{V}$. Application of the principle of virtual work in our coarse-grained morphology constrains the shape, extent and porosity of ridges, assuming each ridge-half is isostatic. The end result is a set of statistical relations for redistribution that can expand the state space of ESMs to include sea ice macroporosity.

The method of coarse-graining of ridges requires three sequential steps: !

1. Determine a morphological description of a ridge that appropriately describes its floating state in terms of mass and volume conservation. In this paper, we chose a simple Euclidean geometry to describe strain, porosity and angle of repose.

2. Choose an appropriate mechanics model to account for the non-conservative vector $\boldsymbol{\mathcal{Q}}$ in the Euler-Lagrange equation so as to permit application of a stationary principle that constrains the porosity and shape of a ridge. We chose Rankine theory because its ap-

plication has a precedent in ridging studies, and it readily lent itself to our variational derivation. Future work may adopt more sophisticated descriptions of self-criticality.

3. Derive ridge frequency statistics for the broader pack that result from quantization of ridging into coarse-grained units. Upon calculating the ridge statistics, a redistribution function and equation of compressive stress may be determined to be applied within Discrete Elements or Eulerian sea ice model cells.

We concede that there are limitations in this adoption of coarse-graining methods for sea ice modeling. The morphological representation of individual ridges is simplistic, and does not match the sophistication of many studies we have cited [e.g. *Hopkins*, 1998; *Kuuliala et al.*, 2017]. Conversely, none of these previous methods are applicable to large scale models. Although we have quantized isostasy over half ridges, and that in itself represents an advance over existing Earth system modeling methods, further steps could permit entirely non-isostatic solutions to occur. We also concede that the presumed Coulombic mechanics assumes that the rubble block sizes within our ridges are considerably smaller than the ridge itself, which is probably false in many small-scale rubble piles, but probably realistic for large ridges. *Hopkins et al.* [1991] noted differences between the Coulombic model predictions and their Discrete Element model of ridge deformation, although they did not explicitly apply a stationary principle, which is the advance of the current study. Statistical relations that emerge from our approach are symptomatic of self criticality that is consistent with scaling relationship we have cited in the sea ice literature.

There are fundamental outcomes from this work that are a product of the variational methods we have used. First and foremost, applying a stationary principle that transcends physical scale helps explain why scaling properties exist in sea ice. When ice ridges, it

passes through four development phases: First the maximum sail height is reached, followed by attainment of maximum keel depth, then outward expansion of the ridge, ending in rearrangement of the ridged rubble field [*Hopkins*, 1998]. Ridging seldom makes it to the third or fourth stage of ridging, and our results agree with this outcome of Hopkins. We have demonstrated mathematically why this might be the case: it is simply energetically preferable to mainly form large numbers of small, underdeveloped ridges rather than populate the surface of polar oceans solely with sparse, large ridges. Consequently, our test case in section 0.10 reveals that heavy straining of an initially uniform sea ice field results in the development of a distribution tail similar to that seen in measurements of ice draft and freeboard. Whereas previous work has looked to physical analogues for ridging to help explain this statistical feature of sea ice, our work suggests that it is an inherent outcome of including porosity prognostically in the thickness distribution, $g(h, \phi_R)$.

We have not addressed in this study the close relationship between ridging and the floe-size distribution, and we leave that aspect of this work for a future assignment. The core motivation leading to this work was to address a problem in our own high-resolution models, the Regional Arctic System Model (RASM) and Energy Exascale Earth System Model (E3SM), whereby the redistribution function and compressive strength of sea ice were not scale aware. That we happened upon a quasi-scaling relationship for ridge evolution akin to descriptions of floe-size is perhaps more than a coincidence, and we intend to explore this result in future work using a discrete element model of sea ice across the Arctic basin.

Arguably the most important bi-product of our investigation is the ability to incorporate the dynamics associated with macroporosity of sea ice into large scale models. It has been

known for some time that this omission has stood in the way of reliable comparisons of Earth system models' sea ice simulations with altimetric retrievals of ice freeboard, including from ICESat [e.g. *Kwok et al.*, 2009] and ICESat-2 [*Markus et al.*, 2017]. We now have the theory required to simulate freeboard in a way that is comparable with satellite retrievals via the equation:

$$\bar{h}_f = \int_0^\infty \int_0^1 \left[h \left(\frac{\rho_w - (1-\phi_R)\rho}{\rho_w} \right) + h_s \left(\frac{\rho_w - (1-\phi_R)\rho_s}{\rho_w} \right) \right] g(h, \phi_R)\, d\phi_R\, dh \quad (51)$$

where $\bar{h}_f$ is mean model freeboard, and it is assumed here that there is a single snow thickness h_s for each ice thickness category in $g(h, \phi_R)$. In our next papers that apply the theory presented in this manuscript, we will use (51) to evaluate our newly-derived method for modeling ice thickness in RASM, E3SM and in a new Discrete Element Model of Sea Ice (DEMSI). This presents an opportunity to test the relationship between strain and macroporosity predicted by the variational method applied to our Coulombic friction model, and to extend our work to understand the impact of snow and thermodynamics on our solution at the basin-scale.

There is a plethora of reasons as to why knowing the state-space of ridges in ESMs is beneficial, aside from knowing macroporosity to aid model validation. Knowing a spectrum of ridges in a model grid cell permits prediction of the roughness of the pack for form drag. Knowing extreme keel depths is useful for modeling fast-ice, which is often pinned by just a few deep keels in contact with continental shelves. Macroporosity provides a mechanism for melt-pond draining unavailable in current ESMs, and is important for the habitat of biota, including for krill in the Southern Ocean. For each of these applications, we now have a dynamical framework for representing distributions of ridges in future

models, and we will work to introduce tracers of ridge quantities into the CICE Consortium model [*Hunke et al.*, 2018] to aid development in this area.

Conclusion

This work has derived a redistribution function of sea ice from first principles in a way that permits extension of the state space of Earth system models to simulate ice macroporosity and ridge state statistics. Our research suggests that macroporosity has an expansionary ridging affect akin to strain that has largely been overlooked in large-scale sea ice dynamics. The Coulombic coarse-graining method we have used to represent macroporous ridges is based on outcomes of a range of modeling and observational studies, and reproduces observed values of ridge shapes through the constraints of a stationary principle applied to our chosen Euler-Lagrange equation of ridging. Ridge statistics of broader deforming sea ice fields naturally emerge from the variational methods used, and explicitly determine the dependence of sea ice density in the pack as a function of deformation scale through the dilation field, $\mathbf{đ}$, that derives from a least action principle. By adopting a variational method that reduces the degrees of freedom associated with ridging, we have opened a potential avenue to multi-scale sea ice simulation.

*Appendices

Equations Describing the Coarse-Grained Ridge Morphology

Euclidean geometric formalisms are often used to describe ridges [e.g. *Kovacs et al.*, 1972; *Tucker and Govoni*, 1981; *Lytle et al.*, 1998; *Worby et al.*, 2008], and have been adapted to simulate fast ice by *Lemieux et al.* [2015] and form drag by *Tsamados et al.* [2014]. These diagnostic applications constrain ridge shapes to particular porosities, sail and keel slopes using isosceles triangles. By contrast, the coarse-grained morphology

described here is different in that it is designed to generate floating ridge state spaces across ϵ_{R_I}, ϕ_R, and α_K for the boundary conditions h_F and h_{F_s} with a more general polygonal description unconstrained by a model's parameter space.

1. Archimedes' Principle

We will analyze ridge cross-sections oriented on the compressional $(\hat{x}, \hat{z})$ plane for consistency with the ridge mechanics described in section 1. Archimedes' Principle and the Mean Value Theorem determine the ridge waterline independent of the shape of the rubble pile, where $\hat{L}_K = L_K / \cos(\pi - \theta_R)$:

$$\rho_w \, h_{R_f} = (\rho_w - \rho) \, h_R + (\rho_w - \rho_s) \, h_{R_s} \tag{1}$$

$$\begin{aligned} \rho_w \, h_{R_d} &= \rho \, h_R + \rho_s \, h_{R_s} \\ &= \frac{2(1-\phi_R)}{\hat{L}_K} \int_0^{\hat{L}_K/2} \left(\rho \, h(\hat{x}, \phi) \, + \rho_s \, h_s(\hat{x}, \phi) \right) d\hat{x} \end{aligned} \tag{2}$$

We are interested in ridge formation, not sustenance, and ignore the possibility that snow mass depresses the ice-snow interface below sea level because this adjustment occurs for level ice prior to ridging. Hence $h_R \geq h_{R_d}$ and $h_{R_s} < h_{R_f}$ where $h_R = h_{R_d} + h_{R_f}$. We assume that ridge rubble is highly permeable, and therefore water and air flows between interlocking ridge fragments and does not affect isostasy. Microporosity within ice blocks and snow associated with brine channels or air pockets is incorporated into their bulk densities, ρ and ρ_s. Therefore the ice and snow thickness sections through the compressional plane of the ridge, h and h_s, are functions both of $\hat{x}$ and the local columnar macroporosity, $\phi(\hat{x})$. Analogous equalities to (1) and (2) give the freeboard and draft of the parent ice

feeding the ridges, h_{Fd} and h_{Ff}, which are only subject to microporosity:

$$\rho_w\, h_{F_f} = (\rho_w - \rho)\, h_F + (\rho_w - \rho_s)\, h_{F_s} \tag{3}$$

$$\rho_w\, h_{F_d} = \rho\, h_F + \rho_s\, h_{F_s} \tag{4}$$

2. Conservation of Volume

As material deforms within the polygonal frame, jumbling ice blocks change the bulk porosity of the ridge such that $h_{Rf}/(1-\phi_R) \geq h_{F_f}$ and $h_{R_d}/(1-\phi_R) \geq h_{F_d}$. Conservation of volume per length of the ridge line in Figure 4, V_R, is given by

$$V_R(\phi_R) = \int_0^{\hat{L}_K/2} \left(h(\hat{x},\phi) + h_s(\hat{x},\phi)\right)\, d\hat{x} = \frac{\hat{L}_k\left(h_{R_f} + h_{R_d}\right)}{2(1-\phi_R)} \tag{5}$$

since h_{R_f} and h_{R_d} account for only the mean thickness of ice within the ridge, excluding cavities between ridge blocks. Equation (5) is a superposition of volume conservation above and below the waterline, which must be individually conserved via Archimedes' Principle in (3) and (4). Therefore conservation of the respective freeboard (f) and draft (d) volume density are given by

$$V_{R_f}(\phi_R)\cos(\pi - \theta_R) = \frac{L_K\, h_{R_f}}{2(1-\phi_R)} = \tfrac{1}{2} h_{F_f}\, L_K + \tfrac{1}{4}\left(H_S - h_{F_f}\right) L_S \tag{6}$$

$$V_{R_d}(\phi_R)\cos(\pi - \theta_R) = \frac{L_K\, h_{R_d}}{2(1-\phi_R)} = \tfrac{1}{2} h_{F_d}\, L_K + \tfrac{1}{4}\left(H_K - h_{F_d}\right) L_K \tag{7}$$

where the right hand equality in each line can be proven geometrically using Figure 3.

3. Conservation of Mass

It follows from (6) and (7) that ice mass is also conserved during deformation. Prior to ridging, deformed ice has a parent sheet thickness h_F and initial width $L_F/2$ of ice to be deformed, which is then horizontally compressed to a final ridge half-width $L_K/2$ with

non-porous mean thickness h_R (Figure 3). Therefore,

$$h_F\, L_F = h_R\, L_K = 2(1-\phi_R)\cos(\pi-\theta_R)\int_0^{\hat{L}_K/2} h(\hat{x},\phi)\, d\hat{x} \tag{8}$$

defines the horizontal Cauchy strain of each ridge half,

$$\epsilon_{R_I}(t_\mathrm{f}) = \frac{L_K(t_\mathrm{f}) - L_F(t_\mathrm{i})}{L_F(t_\mathrm{f})} = \frac{h_F(t_\mathrm{f}) - h_R(t_\mathrm{f})}{h_R(t_\mathrm{f})} = \int_{t_\mathrm{i}}^{t_\mathrm{f}} \dot{\epsilon}_{R_I}\, dt + \epsilon_{R_I}(t_\mathrm{i}) \tag{9}$$

which may be inverted to give the non-porous ridged ice thickness $h_R = h_F/(\epsilon_{R_I}+1)$. Note that in (9) it is assumed that $\epsilon_{R_I}(t_\mathrm{i}) = 0$. Thus compressive strain $\epsilon_{R_I} \in (-1, 0)$ is notably independent of bulk porosity and the slopes of the sail and keel, none of which appear in (9). By the second equality in (9), the total ridge strain may be expressed by sampling the ridge at a single point in time, a consequence of h_F being both an initial and a boundary condition. We choose to use extensional (Cauchy) strain so as to maintain a consistent sign convention with horizontal divergence,

$$\dot{\epsilon}_{R_I} = \frac{1}{\hat{L}_K}\int_0^{\hat{L}_K} \nabla\cdot\hat{v}\; d\hat{x} = \frac{1}{\hat{L}_K}(\hat{v}_{F_b} - \hat{v}_{F_a}), \tag{10}$$

where $\hat{\boldsymbol{v}}(\hat{x},\hat{y},t)$ is the vertically-integrated velocity field within each ridge half. Equation (10) is applicable to symmetric ridges, as in Figure 5a, but is easily expanded for asymmetric ridges such as the one shown in Figure 5b.

Snow mass can only be conserved via ocean coupling not considered here. As jumbling ice blocks disarrange their surface snow within a ridge, a fraction of that snow is submerged and melts into the surrounding sea water. We impose a boundary condition on this process to simplify ridge mechanics, whereby snow remaining on the deformed ice is given the same thickness as snow on the parent ice sheet:

$$h_{R_s} = h_{F_s}. \tag{11}$$

This has a negligible impact on ridge shape (see supplemental material). The associated snow mass per unit ridge-line length transferred to the ocean is:

$$M_{sw} = \rho_s \, L_K \, h_{F_s} \left(\frac{\epsilon_{R_I}}{1 + \epsilon_{R_I}} \right). \tag{12}$$

Snow mass remaining in the ridge is assumed to exist somewhere within the jumbled freeboard volume in Figures 3c, rather than as the organized surface layer seen in Figure 3a.

4. Geometric Constraints

Equations (1)–(7) provide seven equalities for ten variables. Geometric arguments provide the eighth and ninth equations. The morphology is a function of the keel and sail angles of repose, α_K and α_S respectively, where $0 < \alpha_K < \pi/2$ and α_S is limited by the boundary condition $0 < L_S \leq L_K$ which only mildly constrains ridge shape, and includes the specific case of $\alpha_S = \alpha_K$. Varying α_S over $L_S \in (0, L_K]$ has no effect on ridge width nor keel depth because isostasy is determined by and quantized over the keel width L_K, as further explained in the supplementary material. Since α_S has been observed to range only over about $\alpha_K \pm 6^\circ$ [*Timco and Burden*, 1997], we make the simplification $\alpha_S = \alpha_K$. This is often assumed in morphological calculations [e.g., *Tsamados et al.*, 2014] and simplifies the subsequent algebra.

Therefore the ridge extremities may be defined by a single angle of repose on the compressional plane, α_R, such that $\cot\alpha_K = \cos(\pi-\theta_R)\,\cot\alpha_R$:

$$L_S = 2\left(H_S - h_{F_f}\right)\cos(\pi-\theta_R)\,\cot\alpha_R \tag{13}$$

$$L_K = 2\left(H_K - h_{F_d}\right)\cos(\pi-\theta_R)\,\cot\alpha_R \tag{14}$$

$$H_S = h_{F_f} + 2\sqrt{\left(\frac{h_{R_d}}{1-\phi_R} - h_{F_d}\right)\left(\frac{h_{R_f}}{1-\phi_R} - h_{F_f}\right)} \tag{15}$$

$$H_K = \frac{2h_{R_d}}{1-\phi_R} - h_{F_d} \tag{16}$$

Substituting equations (9) and (11) into isostatic relations (1) and (2) further distills L_S, L_K, H_S, and H_K to vary only with the parent ice and snow thickness, h_F and h_{F_s}, and the tensile strain, porosity, compressional angle of repose, and horizontal shearing angle, ϵ_{R_I}, ϕ_R, α_R, and θ_R respectively.

Bivariate Thickness Distribution of a Polygonal Ridge $g_R(h,\phi_R)$

The sectional thickness distribution $g_R(h,\phi_R)$ of the polygonal coarse-grained ridge introduced in section 0.3 is a function of the shortest horizontal distance $\acute{x}$ from the leading edge ($\acute{x}=0$) to the central ridge line ($\acute{x}=L_K/2$) for the porous ice thickness h:

$$h(\acute{x},\phi) = \begin{cases} h_F + \acute{x}\tan\alpha_K; & 0 \le \acute{x} \le \frac{1}{2}(L_K - L_S) \\ h_F + 2\acute{x}\tan\alpha_K - \frac{1}{2}(L_K - L_S)\tan\alpha_K; & \frac{1}{2}(L_K - L_S) < \acute{x} \le \frac{1}{2}L_K \end{cases} \tag{17}$$

and $\acute{x}$ comes from rotation of $\hat{\boldsymbol{x}}(\hat{x},\hat{y},\hat{z})$ by the horizontal shearing angle, θ_R:

$$\begin{bmatrix} \acute{x} \\ \acute{y} \\ \acute{z} \end{bmatrix} = \begin{bmatrix} \cos\theta_R & -\sin\theta_R & 0 \\ \sin\theta_R & \cos\theta_R & 0 \\ 0 & 0 & 1 \end{bmatrix} \begin{bmatrix} \hat{x} \\ \hat{y} \\ \hat{z} \end{bmatrix} \tag{18}$$

given that $\hat{x}$ is aligned with local divergence and the sail and keel angles of repose are equal, as defined in section 0.3.

Temporarily assuming no snow cover, treating $h(\acute{x},\phi)$ as a distribution with respect to $\acute{x}$, inverting equation 17 and employing the change-of-variable technique afforded by

the monotonic increase of h over $\acute{x} \in [0, L_k/2]$ in equation (17),

$$\int_{h_F}^{H_K+H_S} g_R(h, \phi_R)\, dh = \frac{2}{L_K} \int_0^{\frac{L_k}{2}} d\acute{x}(h)$$

gives the bivariate thickness distribution with respect to the cross section of deformed ice that is a function of both h and ϕ_R:

$$g_R(h, \phi_R) = \frac{2}{L_K} \frac{d\acute{x}}{dh} = \frac{\vartheta}{L_K \tan \alpha_K} \tag{19}$$

for the simple step function:

$$\vartheta = \begin{cases} 0; & h < h_F \\ 2; & h_F \leq h \leq h_F + \frac{1}{2}(L_K - L_S) \tan \alpha_K \\ 1; & h_F + \frac{1}{2}(L_K - L_S) \tan \alpha_K < h \leq h_F + \frac{1}{2}(L_K + L_S) \tan \alpha_K \\ 0; & h > h_F + \frac{1}{2}(L_K + L_S) \tan \alpha_K \end{cases}$$

By construction, equation (19) obeys $1 = \int_0^\infty g_R(h, \phi_R)\, dh$ as required for normalized distributions with a single bulk porosity of a ridge ϕ_R. (19) is also applicable to the case with snow cover, since its construction is purely geometric. Substituting for L_K, L_S and α_K in (19) using equations (13) to (16) gives:

$$L_S \tan \alpha_R \sec \theta_R = 2[H_S(\phi_R, \epsilon_{R_I}, h_F, h_{Fs}) - h_{Ff}(h_F, h_{Fs})] \tag{20}$$

$$L_K \tan \alpha_R \sec \theta_R = 2[H_K(\phi_R, \epsilon_{R_I}, h_F, h_{Fs}) - h_{Fd}(h_F, h_{Fs})] \tag{21}$$

Using equations (9) and (11), the relations (20) and (21) reveal that the ridge thickness distribution $g_R(h, \phi_R)$ is a function of the parent ice sheet thickness and snow cover, h_F and h_{Fs}, bulk porosity ϕ_R, and strain ϵ_{R_I}. It is notably independent of shearing angle, θ_R, and angle of repose, α_R. The precise location of the intermediate step on the h-axis changes when α_S deviates from α_K, but only to a minor extent within observed ranges (see

supplemental material). Most importantly, ridge porosity affects the thickness distribution in a similar way to strain, as demonstrated for g_R plotted on the h-plane in Figure 7.

The Lagrangian Density $\mathcal{L}$ of a Polygonal Ridge

In this appendix we derive the Lagrangian density, $\mathcal{L} = \mathcal{T} - \mathcal{V}$ for the coarse-grained ridge morphology introduced in section 0.3 and appendix A. The evolution of $\mathcal{L}$ describes conservative exchanges between kinetic and potential energy densities, $\mathcal{T}$ and $\mathcal{V}$, respectively. We neglect the presence of snow cover due to its limited morphological influence on ridges (see supporting material), but future inclusion of snow into the energetics of ridges described here would be relatively easy. Without snow, $\mathcal{T}$ of a ridge is defined in terms of the mass per unit area of ridging ice, m, and the velocity along the compressional axis of the ridge relative to ice at its extremities, given by $\hat{v}=\hat{v}_{F_b}-\hat{v}_{F_a}$ (Fig. 5). Combining equations (1) to (4), (9) and (10) with relations (13) to (16) results in an equation in terms of ice density $\rho=\rho(\phi_\mu, s, \varepsilon)$, undeformed floe thickness h_F, ridge-wide divergence $\dot{\epsilon}_R$, and the cross-sectional keel width $\hat{L}_K = L_K/\cos(\pi - \theta_R)$:

$$\mathcal{T} = \tfrac{1}{2} m\, \hat{v}^2 = \tfrac{1}{2}\, \rho\, h_F\, \dot{\epsilon}_R{}^2\, \hat{L}_K{}^2 \tag{22}$$

This equality has dimensions [MT^{-2}] and may be expanded to give $\mathcal{T}$ in terms of tensile strain ϵ_{R_I}, macroporosity ϕ_R and angle of repose on the compressional plane α_R, as well as the boundary conditions h_F, $\dot{\epsilon}_R$, and ridge-wide shear, θ_R.

The potential energy density $\mathcal{V}$ of an individual ridge forming along a path may be quantized over polygonal ridge halves. We separate deformed ice thickness (h) into draft (h_d) and freeboard (h_f) on the compressional plane, where $\hat{L}_S = L_S/\cos(\pi - \theta_R)$ for sails

is analogous to $\hat{L}_K$ for keels, and $h(\hat{x},\phi) = h_d(\hat{x},\phi) + h_f(\hat{x},\phi)$:

$$h_d(\hat{x},\phi) = h_{F_d} + \hat{x}\tan\alpha_R \tag{23}$$

$$h_f(\hat{x},\phi) = \begin{cases} h_{F_f}; & 0 \le \hat{x} \le \frac{1}{2}(\hat{L}_K - \hat{L}_S) \\ h_{F_f} + \hat{x}\tan\alpha_R - \frac{1}{2}(\hat{L}_K - \hat{L}_S)\tan\alpha_R; & \frac{1}{2}(\hat{L}_K - \hat{L}_S) < \hat{x} \le \frac{1}{2}\hat{L}_K \end{cases} \tag{24}$$

Following *Rothrock* [1975], the potential energy density of a ridge is the weight of ice, minus the weight of sea water displaced by the ice:

$$\mathcal{V} = 2\int_0^{\hat{L}_K/2}\int_{-h_d}^{h_f} \rho\,\hat{g}(1-\phi_R)\,d\hat{z}\,d\hat{x} - 2\int_0^{\hat{L}_K/2}\int_{-h_d}^{0} \rho_w\,\hat{g}(1-\phi_R)\,d\hat{z}\,d\hat{x}. \tag{25}$$

This equation may be rewritten in terms of $h_d(\hat{x},\phi)$ and $h_f(\hat{x},\phi)$ in (23) and (24):

$$\mathcal{V} = 2\int_0^{\hat{L}_K/2} \Delta\rho\,\hat{g}(1-\phi_R)\,h_d(\hat{x},\phi)\,d\hat{x} - 2\int_0^{\hat{L}_K/2} \rho\,\hat{g}(1-\phi_R)\,h_f(\hat{x},\phi)\,d\hat{x}.$$

recalling that $\Delta\rho{=}\rho_w{-}\rho$. Completing the integration results in potential energy density with dimensions [MT^{-2}]:

$$\mathcal{V} = \Delta\rho\,\hat{g}(1-\phi_R)\Big(h_{F_d}\hat{L}_K + \tfrac{1}{4}\hat{L}_K^{\,2}\tan\alpha_R\Big) + \rho\,\hat{g}(1-\phi_R)\Big(h_{F_f}\hat{L}_K + \tfrac{1}{4}\hat{L}_S^{\,2}\tan\alpha_R\Big). \tag{26}$$

The time-integrated virtual gravitational potential energy density for a ridged ice volume is then $\mathcal{V}(t_\mathrm{f}){-}\mathcal{V}(t_\mathrm{i})$, upon which we may apply $\hat{L}_F{=}\hat{L}_K/(\epsilon_{R_I}+1)$ from (9):

$$\mathcal{V}(t_\mathrm{f}) - \hat{g}\hat{L}_K(\Delta\rho\,h_{F_d} + \rho\,h_{F_f})(\epsilon_{R_I}+1)^{-1} = \int_{t_\mathrm{i}}^{t_\mathrm{f}} \delta\mathcal{V}\,dt \tag{27}$$

Here, the initial potential energy density at t_i is that of an undeformed parent sheet with no macro-porosity that then feeds the ridge up to time t_f. As with equation (22) for $\mathcal{T}$, equation (27) may be further manipulated in order to state $\int_{t_\mathrm{i}}^{t_\mathrm{f}} \delta\mathcal{V}\,dt$ purely in terms of ϵ_{R_I}, ϕ_R, α_R, h_F, and θ_R using the system of equations (1) to (16) in appendix A. This reveals $\mathcal{V}$ to be dependent upon $\cot\alpha_R$, similar to derivations of conservative ridge potential by

Hopkins et al. [1991] and *Kuuliala et al.* [2017]. While not presented here for brevity, the expansion of $\mathcal{V}$ in terms of ϵ_{R_I}, ϕ_R, α_R, h_F, and θ_R along individual ridging paths is used for deriving $\mathcal{Q}_{\hat{x}}$ in section 0.5.3. Subtracting the right hand side of equation (22) from that of (26) gives the Lagrangian density, $\mathcal{L}$.

Derivation of the Angle of Repose $\hat{\alpha}_R$ for Passive Failure

The angle of repose $\hat{\alpha}_R$ of the coarse-grained morphology is obtained by minimizing horizontal compressive stress with respect to α_R, finding ϵ_{R_I} and ϕ_R for:

$$\frac{\partial \sigma_{R\hat{x}}}{\partial \alpha_R} = 0. \tag{28}$$

Drawing on equations (25) through (17) to substitute for $\sigma_{R\hat{x}} = K_p \mathcal{V}_R$, a ridge shape may be determined solely from the potential energy density of the keel, $\mathcal{V}_{R_K}$, because $L_K \geq L_S$. That is, the keel's angle of repose determines the overall shape of the ridge. Both $\mathcal{V}_{R_K}$ and K_p may be expressed in terms of the state variables ϵ_{R_I}, ϕ_R, and α_R and the boundary condition h_F by applying equations (1) through (16). Using equation (26),

$$\begin{aligned} \mathcal{V}_{R_K} &= \hat{g}\Delta\rho(1-\phi_R)\Big(\tfrac{1}{2}\, h_{Fd}\, \hat{L}_K + \tfrac{1}{8}\, \hat{L}_K^{\,2} \tan\alpha_R\Big) \\ &= 2\,\hat{g}\,\Delta\rho\bigg(\frac{\rho}{\rho_w}\bigg)^2 h_F^{\,2}\, \frac{\lambda}{(1-\lambda)(1+\epsilon_{R_I})}\, \cot\alpha_R \end{aligned} \tag{29}$$

where $\lambda = (\phi_R + \phi_R\epsilon_{R_I} - \epsilon_{R_I})$, $\epsilon_{R_I} \in (-1, 0)$ and $\phi_R \in (0, 1)$. Using equations (15) and (16),

$$K_p = \frac{\sqrt{4\,\lambda^2 \cot^2\alpha_R + (1+\lambda)^2} + (1+\lambda)}{\sqrt{4\,\lambda^2 \cot^2\alpha_R + (1+\lambda)^2} - (1+\lambda)}. \tag{30}$$

The roots of the polynomial expansion of $\partial(K_p\, \mathcal{V}_{R_K})/\partial\alpha_R$ then satisfy (28) for the quartic

$$0 = \lambda^2 - (5\lambda^2{+}6\lambda{+}3)\, \varrho^2 + \lambda^2\, \varrho^4 \tag{31}$$

given $\varrho = \tan(\alpha_R/2)$. Only the third root of (31) lies within the physical range $\lambda \in (0, 1)$, hence the angle of repose that assures a state of passive failure for ridging in (20) is

$$\hat{\alpha}_R(\epsilon_{R_I}, \phi_R) = 2 \arctan \sqrt{\frac{(5\lambda^2{+}6\lambda{+}3) - \sqrt{(5\lambda^2{+}6\lambda{+}3)^2 - 4\lambda^4}}{2\lambda^2}} \tag{32}$$

and $\alpha_R = \hat{\alpha}_R(\epsilon_{R_I}, \phi_R)$ is a necessary condition of the modeled system. Substituting for $\hat{\alpha}_R$ in (30) results in an analytic system-wide constant $K_p = 3$, which is within the range $2.4 \leq K_p \leq 4.6$ estimated from discrete element modeling [*Hopkins et al.*, 1991].

*Notation

Acknowledgments.

This work was supported by United States Department of Energy (DOE) grants DESC0005522 and DESC0005783, Office of Naval Research grant N0001417WX00563 and National Science Foundation grants 0612527, 1108542, and 1603602. We are also grateful for support from the DOE Office of Biological and Environmental Research's High-Latitude Application and Testing of Global and Regional Climate Models (HiLAT) project and the Scientific Discovery through Advanced Computing (SciDAC) program. The National Center for Atmospheric Research is sponsored by the National Science Foundation. Developments presented in this paper were influenced by discussions with Peter Wadhams, William Budd, Petra Heil, Adrian Turner, Jennifer Hutchings and Jackie Richter-Menge. The authors thank the Isaac Newton Institute for Mathematical Sciences, Cambridge, for support and hospitality during the Mathematics of Sea Ice Phenomena programme where part of this research was undertaken (EPSRC grant EP/K032208/1). Thanks to Véronique Dansereau and one anonymous reviewer for their excellent com-

ments that greatly improved this manuscript. Supporting audiovisual material [*Roberts*, 2018a] and software [*Roberts*, 2018b] are publicly available at https://zenodo.org.

References

Barnes, G. (2016), *Soil Mechanics: Principles and practice*, fourth ed., 585 pp., Palgrave.

Bedford, A. (1985), *Hamilton's Principle in Continnuum Mechanics*, 107 pp., Pitman Publishing, Ltd.

Bitz, C. M., M. M. Holland, A. J. Weaver, and M. Eby (2001), Simulating the ice-thickness distribution in a coupled climate model, *J. Geophys. Res.*, *106*(C2), 2441–2463, doi: 10.1029/1999JC000113.

Bowen, R. G., and D. R. Topham (1996), A study of the morphology of a discontinuous section of a first year arctic pressure ridge, *Cold Reg. Sci. Technol.*, *24*(1), 83–100, doi:10.1016/0165-232X(95)00002-S.

Cassel, K. W. (2013), *Variational methods with applications in science and engineering*, 413 pp., Cambridge University Press, doi:10.1017/CBO9781139136860.

Castro-Morales, K., F. Kauker, M. Losch, S. Hendricks, K. Riemann-Campe, and R. Gerdes (2014), Sensitivity of simulated Arctic sea ice to realistic ice thickness distributions and snow parameterizations, *J. Geophys. Res. Ocean.*, *119*(1), 559–571, doi: 10.1002/2013JC009342.

Davis, N. R., and P. Wadhams (1995), A statistical analysis of Arctic pressure ridge morphology, *J. Geophys. Res.*, *100*(C6), 10,915–10,925, doi:10.1029/95JC00007.

Doble, M. J., H. Skourup, P. Wadhams, and C. A. Geiger (2011), The relation between Arctic sea ice surface elevation and draft: A case study using coincident AUV sonar

and airborne scanning laser, *J. Geophys. Res.*, *116*, doi:10.1029/2011jc007076.

Ekeberg, O.-C., K. Høyland, and E. Hansen (2015), Ice ridge keel geometry and shape derived from one year of upward looking sonar data in the Fram Strait, *Cold Reg. Sci. Technol.*, *109*, 78–86, doi:10.1016/j.coldregions.2014.10.003.

Flato, G. M., and W. D. Hibler, III (1995), Ridging and strength in modeling the thickness distribution of Arctic sea ice, *J. Geophys. Res.*, *100*(C9), 18,611–18,626, doi:10.1029/95JC02091.

Galley, C. R. (2012), The classical mechanics of non-conservative systems, *Phys. Rev. Lett.*, *110*(4), 1–5, doi:10.1103/PhysRevLett.110.174301.

Galley, C. R., D. Tsang, and L. C. Stein (2014), The principle of stationary nonconservative action for classical mechanics and field theories, *arXiv:1412.3082*, pp. 1–42.

Geiger, C., P. Wadhams, H.-R. Müller, J. Richter-Menge, J. Samluk, T. Deliberty, and V. Corradina (2015), On the uncertainty of sea-ice isostasy, *Ann. Glaciol.*, *56*(69), 341–352, doi:10.3189/2015AoG69A633.

Godlovitch, D., R. Illner, and A. Monahan (2011), Smoluchowski coagulation models of sea ice thickness distribution dynamics, *J. Geophys. Res.*, *116*(C12), doi:10.1029/2011jc007125.

Haas, C., S. Hendricks, H. Eicken, and A. Herber (2010), Synoptic airborne thickness surveys reveal state of Arctic sea ice cover, *Geophys. Res. Lett.*, *37*, doi:10.1029/2010gl042652.

Hamilton, W. R. (1834), On a General Method in Dynamics; By Which the Study of the Motions of All Free Systems of Attracting or Repelling Points is Reduced to the Search and Differentiation of One Central Relation, or Characteristic Function, *Philos. Trans.*

R. Soc. London, *124*, 247–308, doi:10.1098/rstl.1763.0053.

Hamilton, W. R. (1835), Second Essay on a General Method in Dynamics, *Philos. Trans. R. Soc. London*, *125*, 95–144, doi:10.1098/rstl.1835.0009.

Heinonen, J. (2004), Constitutive modeling of ice rubble in first-year ridge keel, *Tech. rep.*, VTT Building and Transport, Finland, Helsinki, Finland.

Hibler, W. D., III (1980), Modeling a variable thickness sea ice cover, *Mon. Weather Rev.*, *108*(12), 1943–1973, doi:10.1175/1520-0493(1980)108$<$1943:MAVTSI$>$2.0.CO;2.

Hopkins, M. A. (1994), On the ridging of intact lead ice, *J. Geophys. Res.*, *99*(C8), 16,351–16,360, doi:10.1029/94JC00996.

Hopkins, M. A. (1998), Four stages of pressure ridging, *J. Geophys. Res.*, *103*(C10), 21,883–21,891, doi:10.1029/98JC01257.

Hopkins, M. A., W. D. Hibler, III, and G. M. Flato (1991), On the numerical simulation of the sea ice ridging process, *J. Geophys. Res.*, *96*(C3), 4809–4820, doi:10.1029/90JC02375.

Horvat, C., and E. Tziperman (2015), A prognostic model of the sea ice floe size and thickness distribution, *Cryosph. Discuss.*, *9*(3), 2955–2997, doi:10.5194/tcd-9-2955-2015.

Høyland, K. V. (2007), Morphology and small-scale strength of ridges in the North-western Barents Sea, *Cold Reg. Sci. Technol.*, *48*(3), 169–187, doi:10.1016/j.coldregions.2007.01.006.

Hunke, E., R. Allard, D. Bailey, A. Craig, A. Damsgaard, F. Dupont, A. Duvivier, M. Holland, N. Jeffery, J.-F. Lemieux, C. Newman, A. Roberts, A. Turner, M. Turner, and M. Winton (2018), CICE-Consortium/CICE: CICE version 6.0.0.alpha, doi:10.5281/zenodo.1205675.

Hunter, S. C. (1983), *Mechanics of continuous media*, 640 pp., Ellis Horwood.

Hutchings, J. K., C. Geiger, A. F. Roberts, J. Richter-Menge, M. Doble, R. Forsberg, K. A. Giles, C. Haas, S. Hendricks, C. Khambhamettu, S. W. Laxon, T. Martin, M. Pruis, M. Thomas, P. Wadhams, and H. J. Zwally (2008), Role of Ice Dynamics in the Sea Ice Mass Balance, *Eos Trans. AGU*, *89*(50), doi:10.1029/2008EO500003.

Hutchings, J. K., A. F. Roberts, and C. Geiger (2011), Spatial and temporal characterization of sea-ice deformation, *Ann. Glaciol.*, *52*(57), 360–368, doi:10.3189/172756411795931769.

Johnston, M., and A. Barker (2000), Microstructure of first year sea ice ridges, *Tech. Rep. HYD-TR-043*, Canadian Hydraulics Center, doi:10.4224/12340979.

Key, J., and A. S. Mclaren (1991), Fractal Nature of the sea ice draft profile, *Geophys. Res. Lett.*, *18*(8), 1437–1440.

Kmiecik, S., D. Gront, M. Kolinski, L. Wieteska, A. E. Dawid, and A. Kolinski (2016), Coarse-Grained Protein Models and Their Applications, *Chem. Rev.*, *116*(14), 7898–7936, doi:10.1021/acs.chemrev.6b00163.

Kovacs, A. (1996), Sea Ice Part II. Estimating the Full-Scale Tensile, Flexural, and Compressive Strength of First-Year Ice, *Tech. rep.*, US Army Corps of Engineers Cold Regions Research & Engineering Laboratory, Hanover, New Hampshire, USA.

Kovacs, A. (1997), Estimating the full-scale flexural and compressive strength of first-year ice, *J. Geophys. Res.*, *102*(C4), 8681–8689, doi:10.1029/96JC02738.

Kovacs, A., W. F. Weeks, S. F. Ackley, and W. D. Hibler, III (1972), A study of a multiyear pressure ridge in the Beaufort Sea, in *AIDJEX Bull. No. 12*, pp. 117–164, University of Washington.

Kuuliala, L., P. Kujala, M. Suominen, and J. Montewka (2017), Estimating operability of ships in ridged ice fields, *Cold Reg. Sci. Technol.*, *135*, 51–61, doi:10.1016/j.coldregions.2016.12.003.

Kwok, R., G. F. Cunningham, M. Wensnahan, I. Rigor, H. J. Zwally, and D. Yi (2009), Thinning and volume loss of the Arctic Ocean sea ice cover: 2003-2008, *J. Geophys. Res.*, *114*, doi:10.1029/2009jc005312.

Lambe, T. W., and R. V. Whitman (1969), *Soil mechanics*, 553 pp., Wiley.

Lanczos, C. (1970), *The variational principles of mechanics*, fourth ed., 418 pp., University of Toronto Press.

Lemieux, J.-F., L. B. Tremblay, F. Dupont, M. Plante, G. C. Smith, and D. Dumont (2015), A basal stress parameterization for modeling landfast ice, *J. Geophys. Res. Ocean.*, *120*(4), 3157–3173, doi:10.1002/2014JC010678.

Leppäranta, M., and R. Hakala (1992), The structure and strength of first-year ice ridges in the Baltic Sea, *Cold Reg. Sci. Technol.*, *20*(3), 295–311, doi:10.1016/0165-232X(92)90036-T.

Lewis, J. E., M. Leppäranta, and H. B. Granberg (1993), Statistical Properties of Sea Ice Surface-Topography in the Baltic Sea, *Tellus Ser. A - Dynamic Meteorol. Oceanogr.*, *45A*(2), 127–142, doi:10.3402/tellusa.v45i2.14865.

Lipscomb, W. H., E. C. Hunke, W. Maslowski, and J. Jakacki (2007), Ridging, strength, and stability in high-resolution sea ice models, *J. Geophys. Res.*, *112*(C03S91), doi:10.1029/2005jc003355.

Lytle, V. I., A. P. Worby, and R. A. Massom (1998), Sea ice pressure ridges in East Antarctica, *Ann. Glaciol.*, *27*, 449–454, doi:10.3189/1998AoG27-1-449-454.

Makarov, S. O. (1901), *Ermak vo l'dakh; opisanie postroiki i plavanii ledokola Ermak i svod nauchnykh materialov, sobrannykh v plavanii*, 507 pp., St. Petersburg, Tipografiia Sanktpetersburgskogo aktsionnogo obshchestvo pechatnogo dela v Rosii E. Evdokimov.

Markus, T., T. Neumann, A. Martino, W. Abdalati, K. Brunt, B. Csatho, S. Farrell, H. Fricker, A. Gardner, D. Hardin, M. Jasinski, R. Kwok, L. Magruder, D. Lubin, S. Luthcke, J. Morison, R. Nelson, A. Neuenschwander, S. Palm, S. Popescu, C. Shum, B. E. Schutz, B. Smith, Y. Yang, and J. Zwally (2017), The Ice, Cloud, and land Elevation Satellite-2 (ICESat-2): Science requirements, concept, and implementation, *Remote Sens. Environ.*, *190*, 260–273, doi:10.1016/j.rse.2016.12.029.

Marsan, D., H. Stern, R. W. Lindsay, and J. Weiss (2004), Scale Dependence and Localization of the Deformation of Arctic Sea Ice, *Phys. Rev. Lett.*, *93*(17), doi: 10.1103/PhysRevLett.93.178501.

Martin, T., M. Tsamados, D. Schroeder, and D. Feltham (2016), The impact of variable sea ice roughness on changes in Arctic Ocean surface stress: A model study, *J. Geophys. Res. Ocean.*, *121*, 1931–1952, doi:10.1002/2015JC011186.

Melling, H., and D. A. Riedel (1995), The Underside Topography of Sea-Ice over the Continental-Shelf of the Beaufort Sea in the Winter of 1990, *J. Geophys. Res.*, *100*(C7), 13,641–13,653. doi:10.1029/95JC00309.

Melling, H., and D. a. Riedel (1996), Development of seasonal pack ice in the Beaufort Sea during the winter of 1991âĂŞ1992: A view from below, *J. Geophys. Res.*, *101*(C5), 11,975, doi:10.1029/96JC00284.

Melling, H., D. R. Topham, and D. Riedel (1993), Topography of the upper and lower surfaces of 10 hectares of deformed sea ice, *Cold Reg. Sci. Technol.*, *21*(4), 349–369,

doi:10.1016/0165-232X(93)90012-W.

Mellor, M. (1980), Ship resistance in thick brash ice, *Cold Reg. Sci. Technol.*, *3*(4), 305–321, doi:10.1016/0165-232X(80)90037-3.

Mellor, M. (1986), Mechanical Behavior of sea ice, in *The geophysics of sea ice*, edited by N. Untersteiner, pp. 165–281, Plenum Press.

Moslet, P. O. (2007), Field testing of uniaxial compression strength of columnar sea ice, *Cold Reg. Sci. Technol.*, *48*(1), 1–14, doi:10.1016/j.coldregions.2006.08.025.

Noid, W. G., J. W. Chu, G. S. Ayton, V. Krishna, S. Izvekov, G. A. Voth, A. Das, and H. C. Andersen (2008), The multiscale coarse-graining method. I. A rigorous bridge between atomistic and coarse-grained models, *J. Chem. Phys.*, *128*(24), doi:10.1063/1.2938860.

Nuber, A., L. Rabenstein, J. A. Lehmann-Horn, M. Hertrich, S. Hendricks, A. Mahoney, and H. Eicken (2013), Water content estimates of a first-year sea-ice pressure ridge keel from surface-nuclear magnetic resonance tomography, *Ann. Glaciol.*, *54*(64), 33–43, doi:10.3189/2013AoG64A205.

Paget, M. J., A. P. Worby, and K. J. Michael (2001), Determining the floe-size distribution of East Antarctic sea ice from digital aerial photographs, *Ann. Glaciol.*, *33*, 94–100, doi:10.3189/172756401781818473.

Parmerter, R. R., and M. D. Coon (1972), Model of pressure ridge formation in sea ice, *J. Geophys. Res.*, *77*(33), 6565–6575, doi:10.1029/JC077i033p06565.

Perovich, D. K., and K. F. Jones (2014), The seasonal evolution of sea ice floe size distribution, *J. Geophys. Res. Ocean.*, *119*(12), 8767–8777, doi:10.1002/2014JC010136.

Petty, A. A., M. C. Tsamados, N. T. Kurtz, S. L. Farrell, T. Newman, J. P. Harbeck, D. L. Feltham, and J. A. Richter-Menge (2016), Characterizing Arctic sea ice topography using high-resolution IceBridge data, *Cryosphere*, *10*(3), 1161–1179, doi:10.5194/tc-10-1161-2016.

Pringle, D. J., J. E. Miner, H. Eicken, and K. M. Golden (2009), Pore space percolation in sea ice single crystals, *J. Geophys. Res.*, *114*(C12), doi:10.1029/2008jc005145.

Roach, L. A., C. Horvat, S. M. Dean, and C. M. Bitz (2018), An Emergent Sea Ice Floe Size Distribution in a Global Coupled Ocean-Sea Ice Model, *J. Geophys. Res. Ocean.*, *123*(6), 4322–4337, doi:10.1029/2017JC013692.

Roberts, A. F. (2018a), Audiovisual Vignettes of Sea Ice Ridging in the Beaufort Sea in 2007 (Version 2), *Zenodo*, doi:10.5281/zenodo.1252414.

Roberts, A. F. (2018b), Ridgepack, Version 1.0.1, *Zenodo*, doi:10.5281/zenodo.2477370.

Rothrock, D. A. (1975), The energetics of the plastic deformation of pack ice by ridging, *J. Geophys. Res.*, *80*(33), 4514–4519, doi:10.1029/JC080i033p04514.

Stern, H. L., and R. W. Lindsay (2009), Spatial scaling of Arctic sea ice deformation, *J. Geophys. Res.*, *114*(C10), 1–10, doi:10.1029/2009JC005380.

Strub-Klein, L., and D. Sudom (2012), A comprehensive analysis of the morphology of first-year sea ice ridges, *Cold Reg. Sci. Technol.*, *82*, 94–109, doi:10.1016/j.coldregions.2012.05.014.

Strutt, J. W. L. R. (1871), Some general theorems relating to vibrations, *Proc. London Math. Soc.*, *1-4*, 357–368, doi:10.1112/plms/s1-4.1.357.

Tan, B., Z. J. Li, P. Lu, C. Haas, and M. Nicolaus (2012), Morphology of sea ice pressure ridges in the northwestern Weddell Sea in winter, *J. Geophys. Res. Ocean.*, *117*(6),

1–13, doi:10.1029/2011JC007800.

Thorndike, A. S., D. A. Rothrock, G. A. Maykut, and R. Colony (1975), The thickness distribution of sea ice, *J. Geophys. Res.*, *80*(33), 4501–4513, doi:10.1029/JC080i033p04501.

Timco, G., and W. Weeks (2010), A review of the engineering properties of sea ice, *Cold Reg. Sci. Technol.*, *60*(2), 107–129, doi:10.1016/j.coldregions.2009.10.003.

Timco, G., K. Croasdale, and B. Wright (2000), An Overview of First-Year Sea Ice Ridges, *Tech. rep.*, Canadian Hydraulics Center, Ottawa, Ontario, Canada.

Timco, G. W., and R. P. Burden (1997), An analysis of the shapes of sea ice ridges, *Cold Reg. Sci. Technol.*, *25*, 65–77, doi:10.1016/S0165-232X(96)00017-1.

Toppaladoddi, S., and J. S. Wettlaufer (2015), Theory of the Sea Ice Thickness Distribution, *Phys. Rev. Lett.*, *115*(14), 2–5, doi:10.1103/PhysRevLett.115.148501.

Tsamados, M., D. L. Feltham, D. Schröder, D. Flocco, S. L. Farrell, N. Kurtz, S. W. Laxon, and S. Bacon (2014), Impact of Variable Atmospheric and Oceanic Form Drag on Simulations of Arctic Sea Ice, *J. Phys. Oceanogr.*, *44*(5), 1329–1353, doi:10.1175/JPO-D-13-0215.1.

Tucker, W. B., III, and J. W. Govoni (1981), Morphological investigations of first-year sea ice pressure ridge sails, *Cold Reg. Sci. Technol.*, *5*(1), 1–12, doi:10.1016/0165-232X(81)90036-7.

Tucker, W. B., III, D. S. Sodhi, and J. W. Govoni (1984), Structure of first-year pressure ridge sails in the Prudhoe Bay Region, *Alaskan Beaufort Sea Ecosyst. Environ.*, P. W. Barnes, D. M. Schell and E. Reimnitz *eds.*, 115–135, Academic Press.

Turner, A. K., and E. C. Hunke (2015), Impacts of a mushy-layer thermodynamic approach in global sea-ice simulations using the CICE sea-ice model, *J. Geophys. Res.*,

120, 1253–1275, doi:10.1002/2014JC010358.

Ungermann, M., L. B. Tremblay, T. Martin, and M. Losch (2017), Impact of the ice strength formulation on the performance of a sea ice thickness distribution model in the Arctic, *J. Geophys. Res. Ocean.*, *122*(3), 2090–2107, doi:10.1002/2016JC012128.

Vancoppenolle, M., T. Fichefet, and H. Goosse (2009), Simulating the mass balance and salinity of Arctic and Antarctic sea ice. 2. Importance of sea ice salinity variations, *Ocean Model.*, *27*(1-2), 54–69, doi:10.1016/J.Ocemod.2008.11.003.

Virga, E. G. (2015), Rayleigh-Lagrange formalism for classical dissipative systems, *Phys. Rev. E - Stat. Nonlinear, Soft Matter Phys.*, *91*(1), doi:10.1103/PhysRevE.91.013203.

Wadhams, P. (1988), The underside of Arctic sea ice imaged by sidescan sonar, *Nature*, *333*(6169), 161–164, doi:10.1038/333161a0.

Wadhams, P., and N. Davis (1994), The fractal properties of the underside of Arctic sea ice, *Trans. Built Environ.*, *5*, 353–363, doi:10.2495/CMO940351.

Wadhams, P., and T. Davy (1986), On the spacing and draft distributions for pressure ridge keels, *J. Geophys. Res.*, *91*(C9), 10,697, doi:10.1029/JC091iC09p10697.

Wadhams, P., and M. J. Doble (2008), Digital terrain mapping of the underside of sea ice from a small AUV, *Geophys. Res. Lett.*, *35*(1), 4–9, doi:10.1029/2007GL031921.

Wadhams, P., M. A. Lange, and S. F. Ackley (1987), The ice thickness distribution across the Atlantic sector of the Antarctic Ocean in mid-winter, *J. Geophys. Res.*, *96*(C13), 14,535–14,552, doi:10.1029/JC092iC13p14535.

Wadhams, P., N. Hughes, and J. Rodrigues (2011), Arctic sea ice thickness characteristics in winter 2004 and 2007 from submarine sonar transects, *J. Geophys. Res.*, *116*, doi:10.1029/2011jc006982.

Wan, F. Y. (1995), *Introduction to the calculus of variations and its applications*, 638 pp., Chapman and Hall.

Webster, M., I. G. Rigor, S. V. Nghiem, N. T. Kurtz, S. L. Farrell, D. K. Perovich, and M. Sturm (2014), Interdecadal changes in snow depth on Arctic sea ice, *J. Geophys. Res. Ocean.*, pp. n/a–n/a, doi:10.1002/2014JC009985.

Weeks, W. F. (2010), *On Sea Ice*, 664 pp., University of Alaska Press.

Weiss, J. (2001), Fracture and fragmentation of ice: A fractal analysis of scale invariance, *Eng. Fract. Mech.*, *68*(17-18), 1975–2012, doi:10.1016/S0013-7944(01)00034-0.

Weiss, J. (2003), Scaling of Fracture and Faulting of Ice on Earth, *Surv. Geophys.*, *24*(2), 185–227, doi:10.1023/A:1023293117309.

Worby, A. P., M. O. Jeffries, W. F. Weeks, K. Morris, and R. Jana (1996), The thickness distribution of sea ice and snow cover during late winter in the Bellingshausen and Amundsen Seas, Antarctica, *J. Geophys. Res.*, *101*(C12), 28,411–28,455, doi:10.1029/96JC02737.

Worby, A. P., C. A. Geiger, M. J. Paget, M. L. Van Woert, S. F. Ackley, and T. L. DeLiberty (2008), Thickness distribution of Antarctic sea ice, *J. Geophys. Res.*, *113*(C5), doi:10.1029/2007jc004254.

Zhang, J., and D. A. Rothrock (2003), Modeling global sea ice with a thickness and enthalpy distribution model in generalised curvilinear coordinates, *Mon. Weather Rev.*, *131*(5), 845–861, doi:10.1175/1520-0493(2003)131$<$0845:MGSIWA$>$2.0.CO;2.

Zubov, N. N. (1945), *L'dy Arktiki*, 491 pp., Izdatel'stvo Glavsevmorputi, Moscow, Russia (1963 English translation 'Arctic Ice' by U.S. Navy Electronics Laboratory, San Diego, California, USA, 510pp).

Table 1. Constants

Symbol	Definition	Value
ρ	Density of floe ice	917 kg m^{-3}
ρ_s	Density of snow	330 kg m^{-3}
ρ_w	Density of sea water	1026 kg m^{-3}
$\Delta\rho$	Sea water and sea ice density difference ($\rho_w - \rho$)	109 kg m^{-3}
$\hat{g}$	Acceleration due to Earth's gravity	9.8 m s^{-2}

Table 2. Apparent mean observed quantities of angle of keel repose, $\alpha_{K_{\text{obs}}}$ and porosity $\phi_{R_{\text{obs}}}$ as would occur if a 5 m cutoff were applied to ridges predicted by b_R in equation (45), so as to mimic processing of sonar retrievals by *Davis and Wadhams* [1995]. Values are categorized according to the deforming parent ice thickness, h_F, and values highlighted in blue provide the true mean values predicted by b_R, but would only be seen in sonar processing where a keel draft H_K exceeds 5m for all ridges produced by a parent sheet.

h_F (m)	0.20	0.50	1.00	2.00	5.00	$H_K > 5$ m
$\alpha_{K_{\text{obs}}}$	29.3°	28.2°	26.4°	22.9°	11.8°	10.4°
$\phi_{R_{\text{obs}}}$	0.36	0.35	0.31	0.24	0.10	0.09

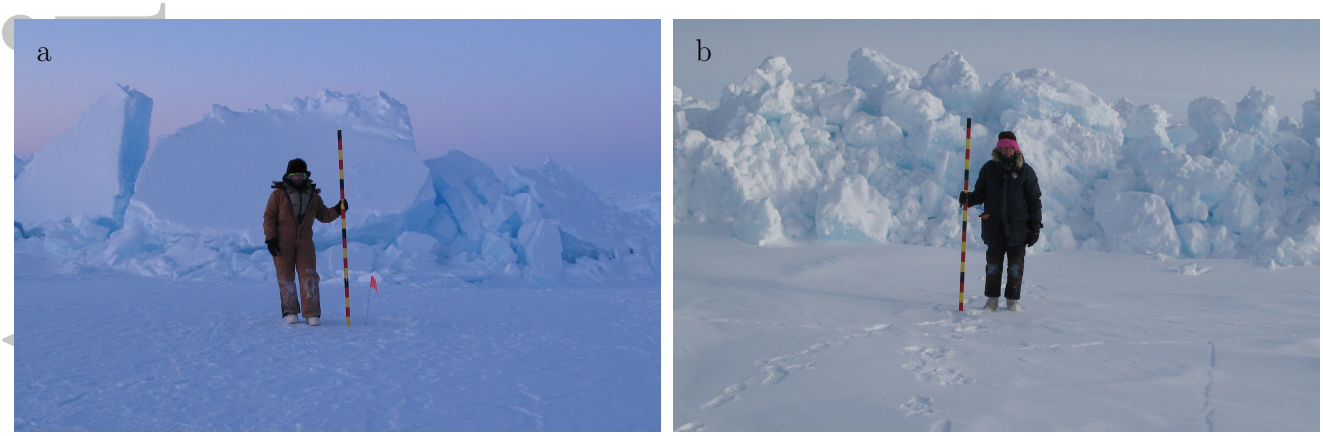

Figure 1. Ridges surveyed as part of the Sea Ice Experiment - Dynamic Nature of the Arctic (SEDNA) field campaign in the Beaufort Sea [*Hutchings et al.*, 2008, 2011]: a) A pressure ridge photographed on April 9, 2007 UTC near 73.21°N, 146.65°W, and included in the autonomous keel measurements of *Wadhams and Doble* [2008]; b) Shear ridge measured on April 7, 2007 UTC near 73.34°N, 146.11°W. The gauge stick is 2 m high, graded at 0.1 m intervals, and approximately 2 m from the base of the sail. The camera position is 10 m from the sail base.

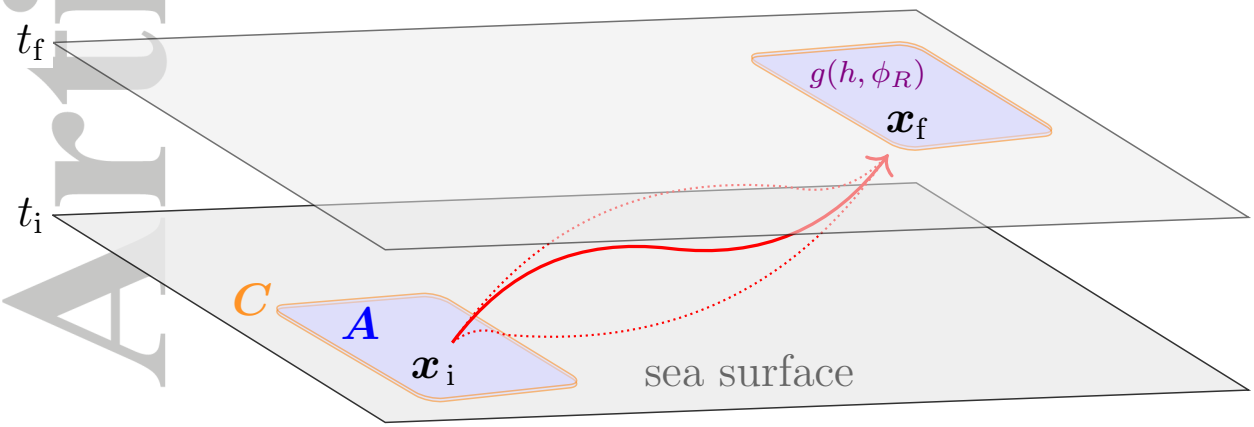

Figure 2. Schematic of a path $\boldsymbol{x}=\chi(\boldsymbol{X}, t)$ (solid red) and possible variations of that path (dotted red) over an area A of the pack with perimeter C drifting and ridging between the initial location $\boldsymbol{x}_i$ and final position $\boldsymbol{x}_f$ at time t_i and t_f, respectively. The bivariate thickness distribution $g(h, \phi_R)$ evolves over the course of the drift path, and may describe an area of just one ridging event, or an aggregation of many.

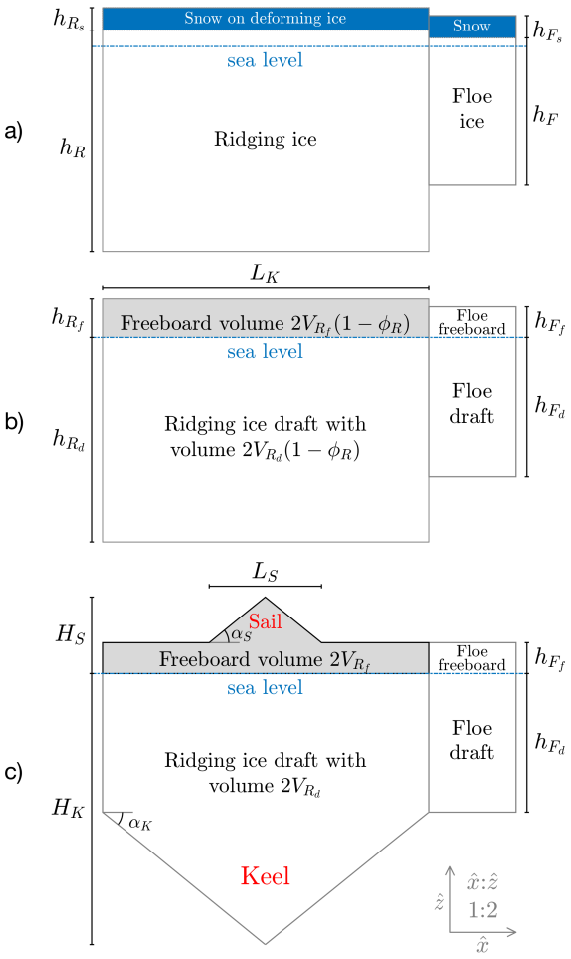

Figure 3. Developmental cross-section of the polygonal isostatic ridge model. Imporous metrics for ridged and adjacent level ice and snow are illustrated in (a). The associated metrics for sea ice draft and freeboard appear in (b), which has a total cross sectional volume density $2V_R(1-\phi_R)$, where ϕ_R is the bulk porosity of the ridge in (c). This schematic presents the special case of ϕ_R=0 so that the horizontal extent L_K in (c) is equal to that of the imporous ridged mass in (a) and (b). The angle of repose of the symmetric keel and sail are identical (α_K=α_S) and equal to 22° for consistency with subsequent figures. There is no ridge shear (θ_R=180°). Each frame is to scale and has a horizontal ($\hat{x}$) to vertical ($\hat{z}$) aspect ratio of 1:2, where h_F=2 m, h_{Fs}=0.3 m, and $\epsilon_{R_I} = -1/3$.

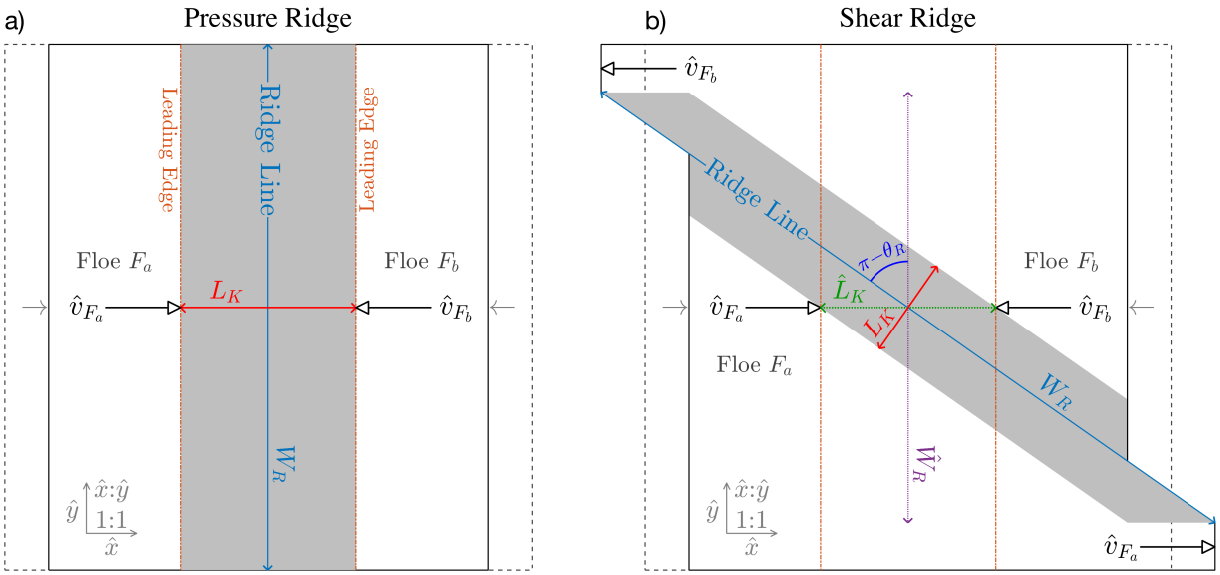

Figure 4. Orthographic plan-view of the polygonal isostatic ridge model for (a) pressure and (b) shear ridging. The $\hat{x}$-axis is aligned with extensional ridge strain, ϵ_{R_I}, and the $\hat{y}$-axis is aligned with horizontal shear strain ($\epsilon_{R_I} \tan\theta_R$). The black dashed box in (a) and (b) is the initial outline of two colliding floe segments with velocities $\hat{v}_{F_a}$ and $\hat{v}_{F_b}$ relative to the ridge line. Solid black lines indicate the final floe segments after ridging, where the cross-sectional ridge profile along L_K casts an angle $\pi-\theta_R$ with the $\hat{x}$-axis, which is the angle between the pressure and shear ridge lines in (a) and (b). Both frames share identical horizontal scales and a square aspect ratio. The gray-shaded symmetric ridge extent in (a) corresponds to the cross-sections in Figures 5a and 9a (L_K=15.7 m, θ_R=180°). Equivalently, (b) is the plan view of the shear ridge profile in Figure 9b (L_K=9.0 m, θ_R=125°). $\epsilon_{R_I} = -1/3$ for both (a) and (b).

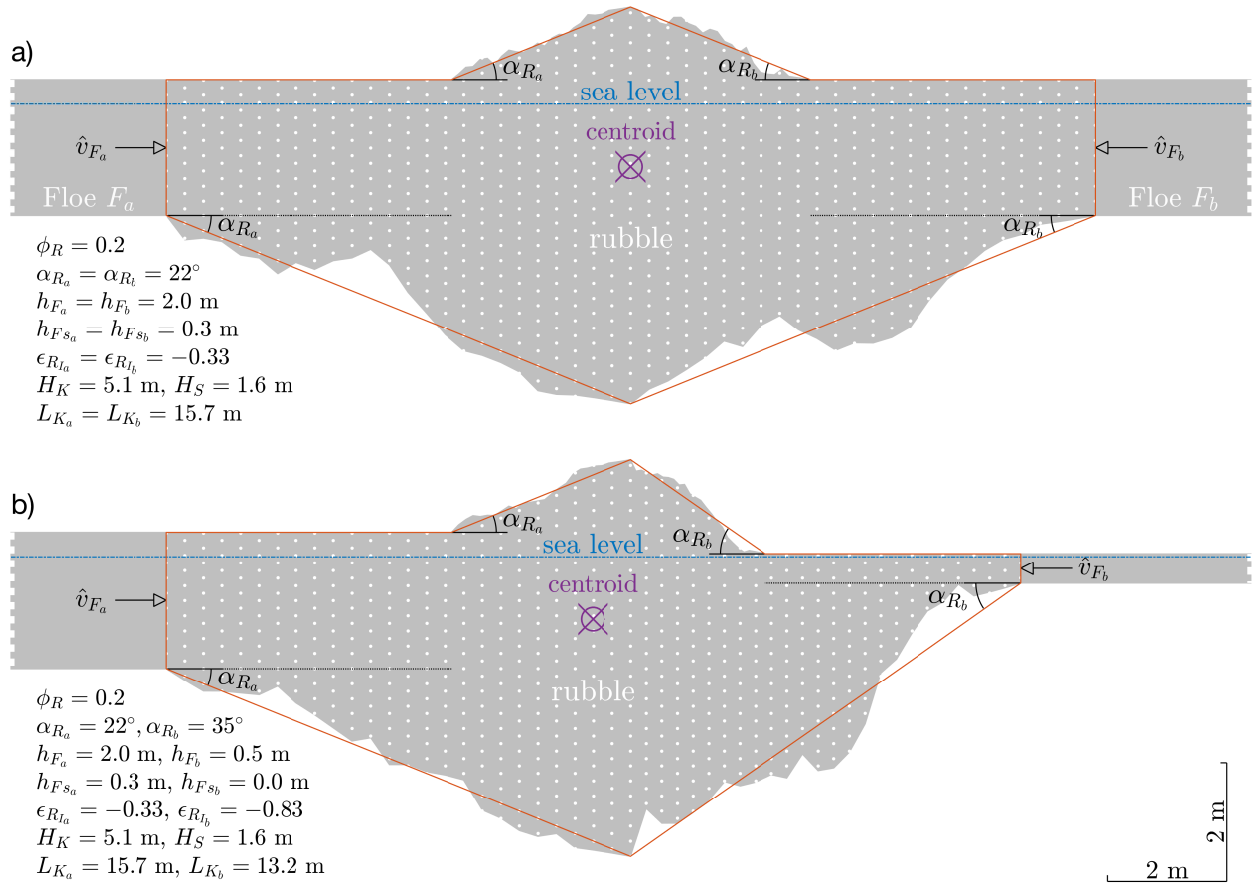

Figure 5. Orthographic cross-section of (a) symmetric and (b) asymmetric pressure ridges (θ_R=180°) within an isostatic polygonal frame joined along the transect connecting the level ice boundary with the peak sail height and keel depth (orange frame). The randomly generated ice and snow volume (gray section) has a symmetric mass either side of the centroid and has uniform bulk porosity, ϕ_R. Half-width metrics refer to the left (F_a, R_a) and right (F_b, R_b) floes and ridge-halves, including the horizontal parent sheet velocities, $\hat{v}_{F_{a,b}}$, relative to the centroid. The ridge in (a) is identical to that in Figure 3c, except here it is 20% porous. A plan view of (a) can be seen in Figure 4a. Both (a) and (b) share the same scale and a square $\hat{x}$:$\hat{z}$ aspect ratio. Stippling signifies the zone of macroporosity.

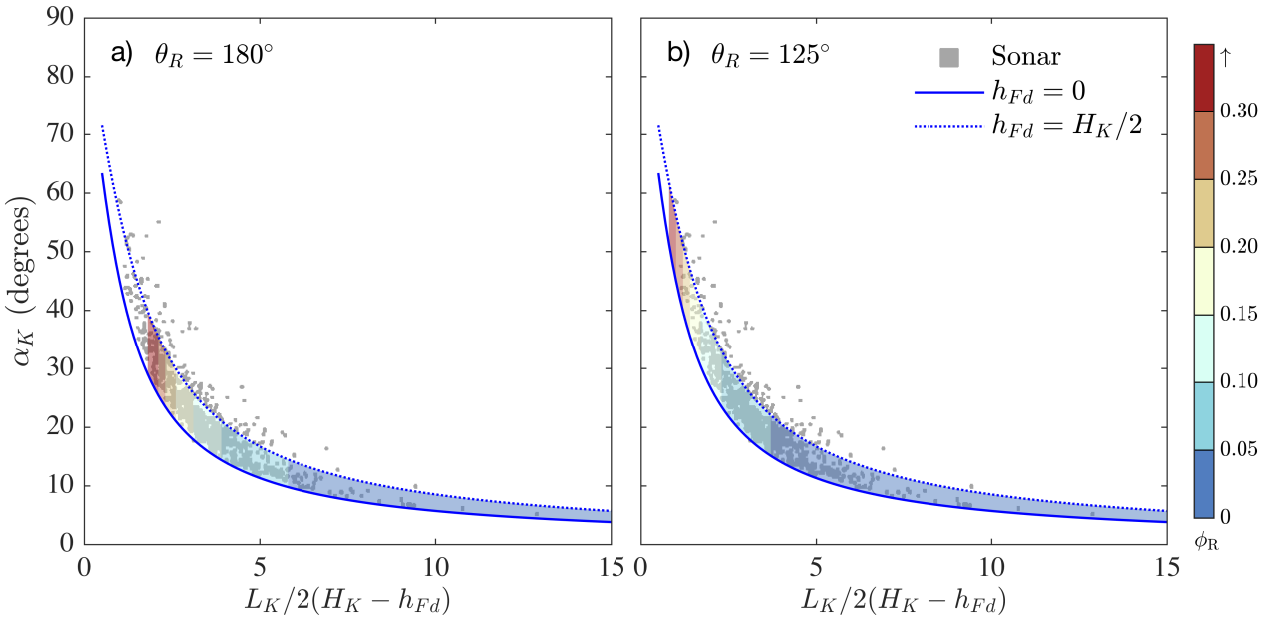

Figure 6. Comparison between the coarse-grained ridge shape (blue lines) and *Davis and Wadhams* [1995] sonar analysis of 729 independent keels with drafts between 5 and 29 m (gray scatter). Color shading indicates bulk macroporosity of the keel as predicted by the stationary principle in equation (32) for (a) pressure ridging and (b) horizontal shearing of the same magnitude as in Figure 4b. $L_K/2(H_K - h_{F_d})$ is the keel half-width-to-depth ratio relative to the level ice base, and α_K is the keel angle of repose, irrespective of shear, hence the blue traces and scatter graphs are identical in both (a) and (b).

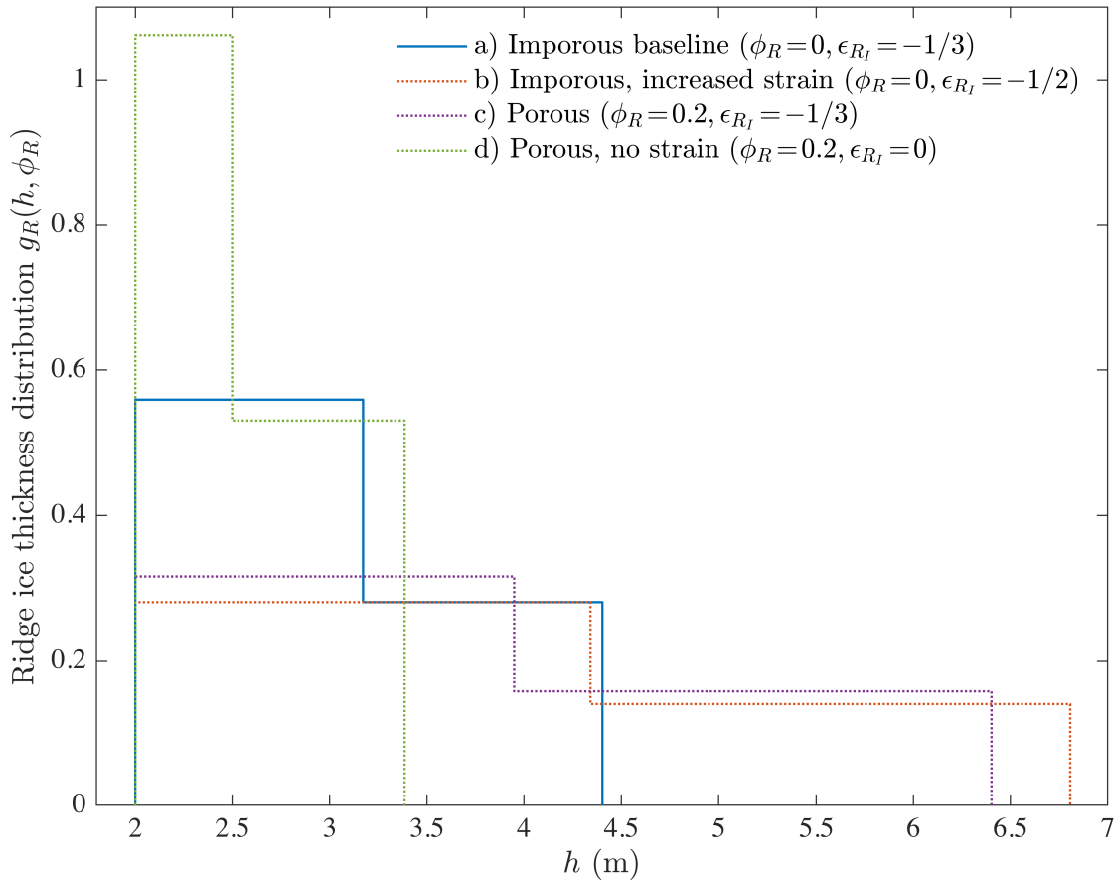

Figure 7. The ice thickness distribution normalized over coarse-grained ridge widths, $g_R(h, \phi_R)$, with parent ice sheet thickness h_F=2.0 m and snow cover h_{Fs}=0.3 m, as represented on the h-axis. Ridge states (a) through (d) are identical in this figure as for the respective polygons of the ridgegraph in Figure 8, and share the same color code.

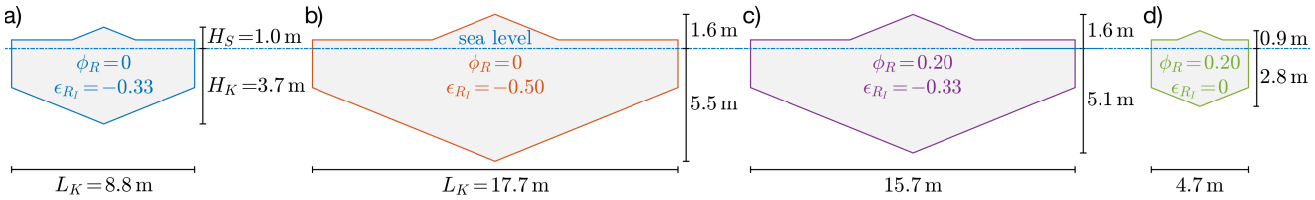

Figure 8. Ridgegraph of coarse-grained symmetric pressure ridges corresponding to the $g_R(h, \phi_R)$ distributions in Figure 7 for the given strain, ϵ_{R_I}, and bulk porosity, ϕ_R: a) Baseline case, which is a reproduction of Figure 3c, with zero porosity and strain ϵ_{R_I}=−1/3; b) Identical to the baseline except that ridge strain has increased to ϵ_{R_I}=−1/2; c) Identical to the baseline except that ridge porosity has increased to ϕ_R=0.2, identical to Figure 5a; d) Strain is set to zero, and porosity is ϕ_R=0.2, equivalent to the case of horizontally static sea ice fracture. All ridges share the same parent floes (h_{Fi}=2 m, h_{Fs}=0.3 m), angle of repose (α_R=22°) and are each pressure ridges (θ_R=180°). Color coding corresponds to the step functions in Figure 7.

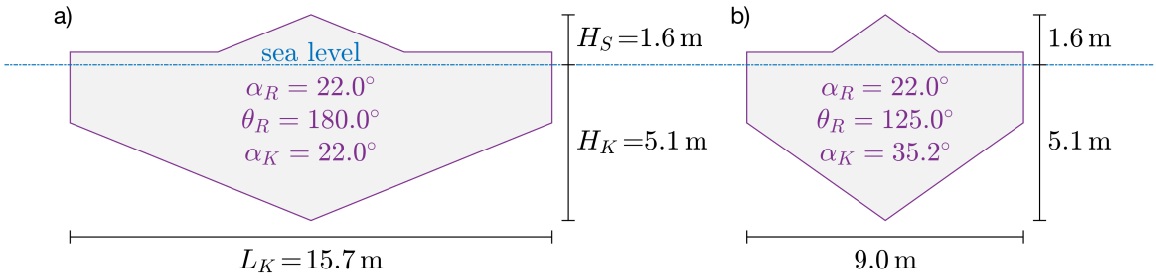

Figure 9. Ridgegraph of coarse-grained symmetric relief under (a) compressional stress and (b) a combination of shear and convergence. (a) is a reproduction of the pressure ridge in Figure 5a (θ_R=180°), with boundary conditions h_{Fi}=2 m and h_{Fs}=0.3 m, compressional angle of repose α_R=22°, porosity ϕ_R=0.2 and strain ϵ_{R_I}=−1/3. (b) is a ridge formed under identical conditions to (a), except with a portion of shear (θ_R=125°). Respective ridges cross-sections in this figure fall along the red transects denoted 'L_K' in Figure 4a and 4b plan views, and both ridges (a) and (b) share the same $g_R(h, \phi_R)$ distribution in Figure 7, trace (c).

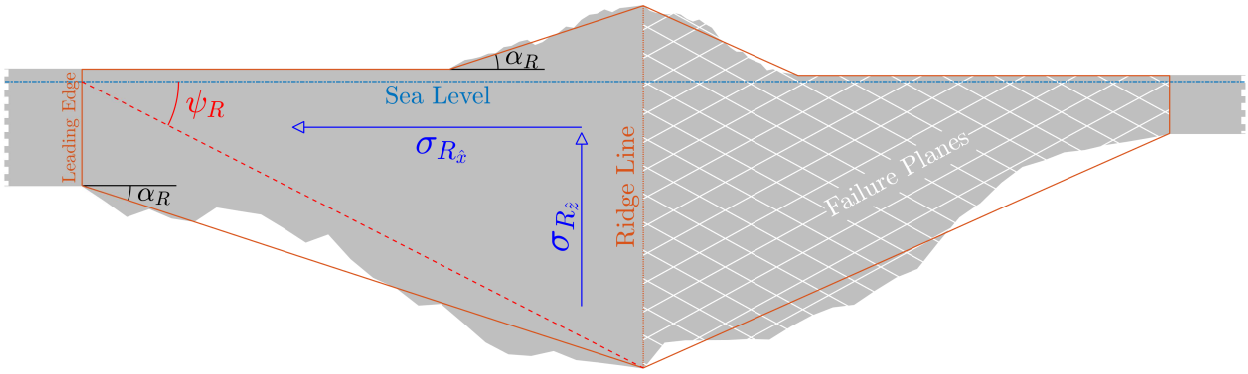

Figure 10. Coarse-grained Coulombic friction model used to determine constraints on the shape and extent of sea ice ridges. The respective horizontal ($\sigma_{R_{\hat{x}}}$) and vertical ($\sigma_{R_{\hat{z}}}$) stress terms on the compressional $(\hat{x}, \hat{z})$ plane for a ridge half are annotated in blue. The critical angle of friction ψ_R is the acute tilt of failure planes relative to the sea surface for which the ridge is in equilibrium, annotated for the principle plane for one ridge half (red) and all failure planes relevant to the other ridge half (white).

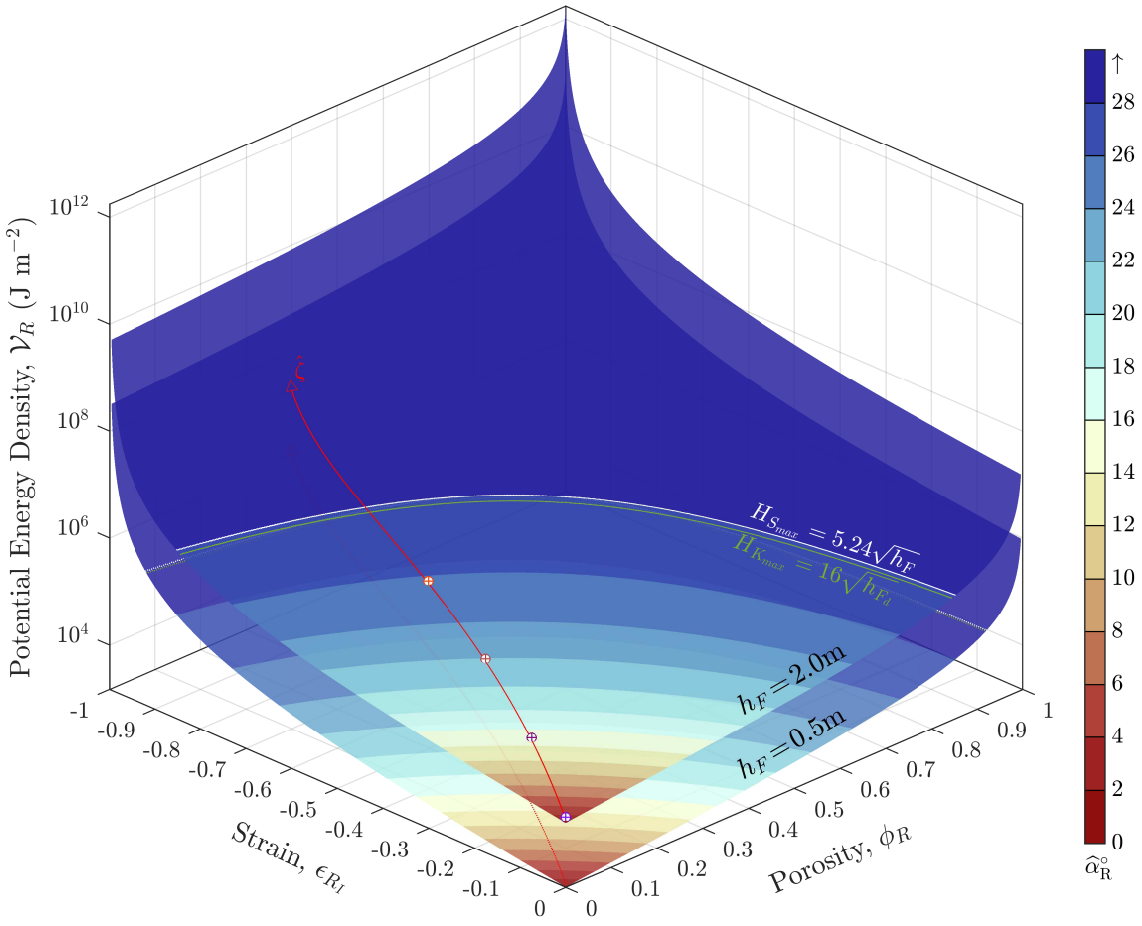

Figure 11. Surfaces of the potential energy density $\mathcal{V}_R$=$\mathcal{V}(\epsilon_{R_I}, \phi_R, \hat{\alpha}_R, h_F)$ for parent ice sheets feeding a ridge with thicknesses of 0.5 and 2.0 m. Color shading indicates the angle of repose $\hat{\alpha}_R$ of ridge states for which $\partial_{\alpha_R}\sigma_{R\hat{x}}$=0. White and green lines are the coarse-grained ridge states matching empirical approximations of maximum sail height and keel depth by *Tucker et al.* [1984] and *Melling and Riedel* [1996], respectively. Red streamlines indicate the ridging trajectory $\hat{\boldsymbol{\zeta}}$ for which $\nabla_R \cdot \mathbf{d}$=0. Color markings along the h_F=2.0 m solid red state-space trajectory correspond to the locations of $a_R(h, \phi_R, \boldsymbol{x})$ steps in Figure 13.

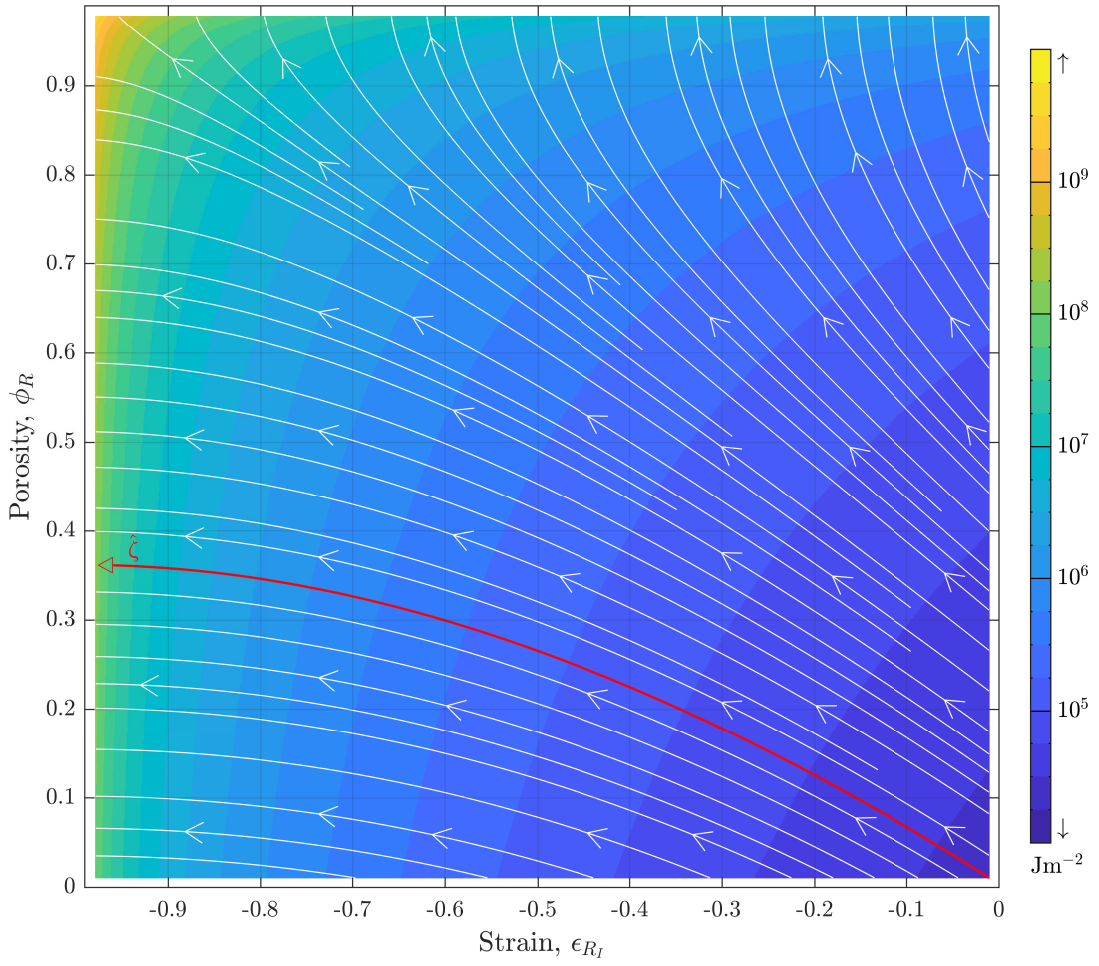

Figure 12. The dilation field $\mathbf{đ}$ (white streamlines) of the h_F=2.0 m surface of $\mathcal{V}_R$ in Figure 11, color shaded according to gravitational potential energy density ($\mathcal{V}$). The solid red streamline is identical to the $\hat{\zeta}$ state space trajectory in Figure 11 and is orthogonal to $\mathcal{V}$ contours. $\hat{\zeta}$ passes through the initial condition $\zeta_0(\epsilon_{R_I}, \phi_R)$=$(0, 0)$ for ridge strain ϵ_{R_I} and porosity ϕ_R.

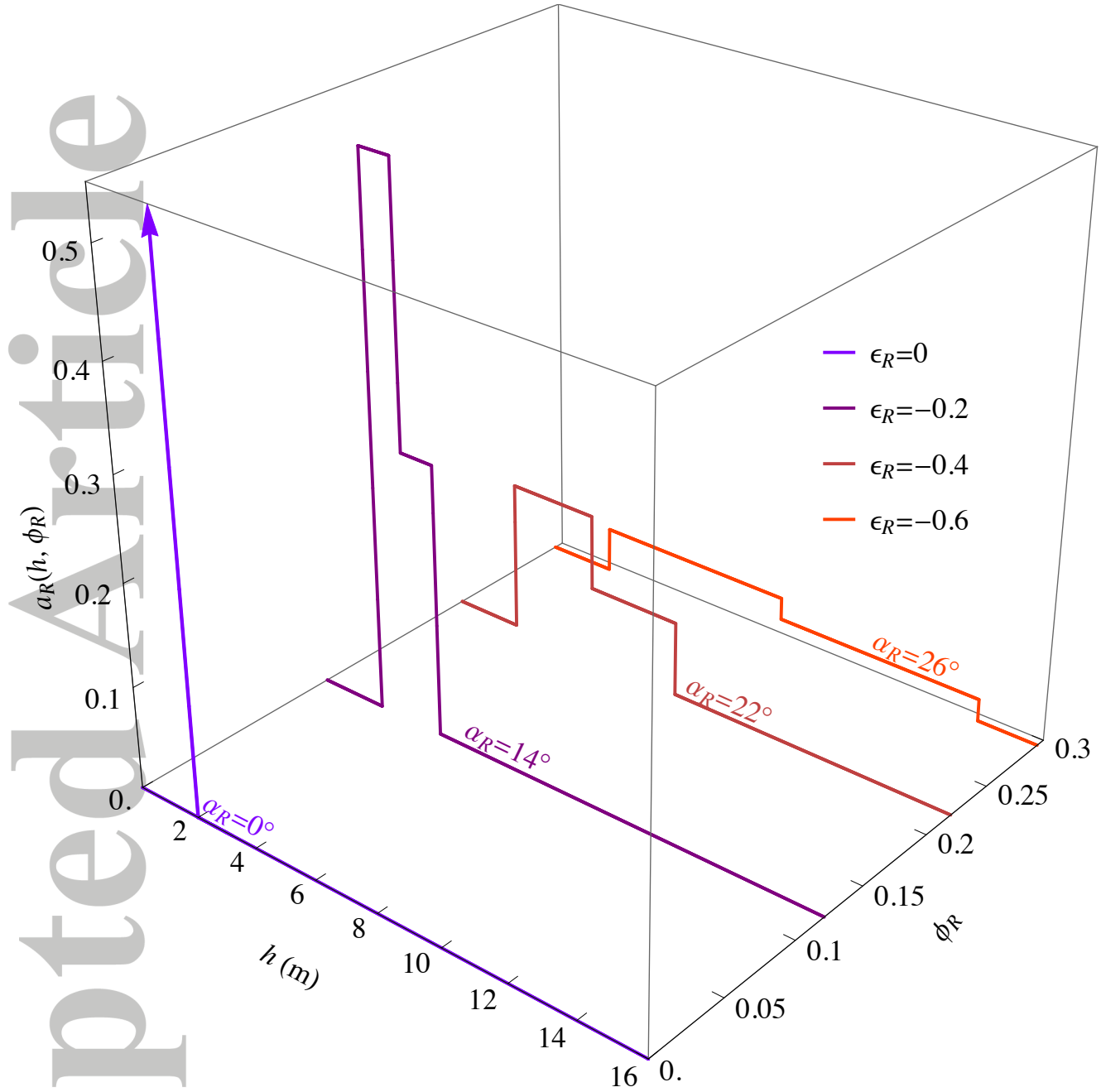

Figure 13. Bivariate sea ice thickness distribution $a_R(h, \phi_R, \boldsymbol{x})$ of an individual coarse-grained ridge formed from a parent ice sheet 2 m thick under progressively greater compressive strain (ϵ_{R_I}) from which porosity (ϕ_R) and angle of repose (α_R) are obtained from the $\hat{\boldsymbol{\zeta}}$ trajectory derived in section 0.7.3. Step functions in this figure correspond to the color-marked state-space locations along the solid red $\hat{\boldsymbol{\zeta}}$ streamline in the $\mathcal{V}_R$ in Figure 11. The upward arrow on the ϵ_{R_I}=0 distribution indicates a Dirac delta function for ν_F=2 m.

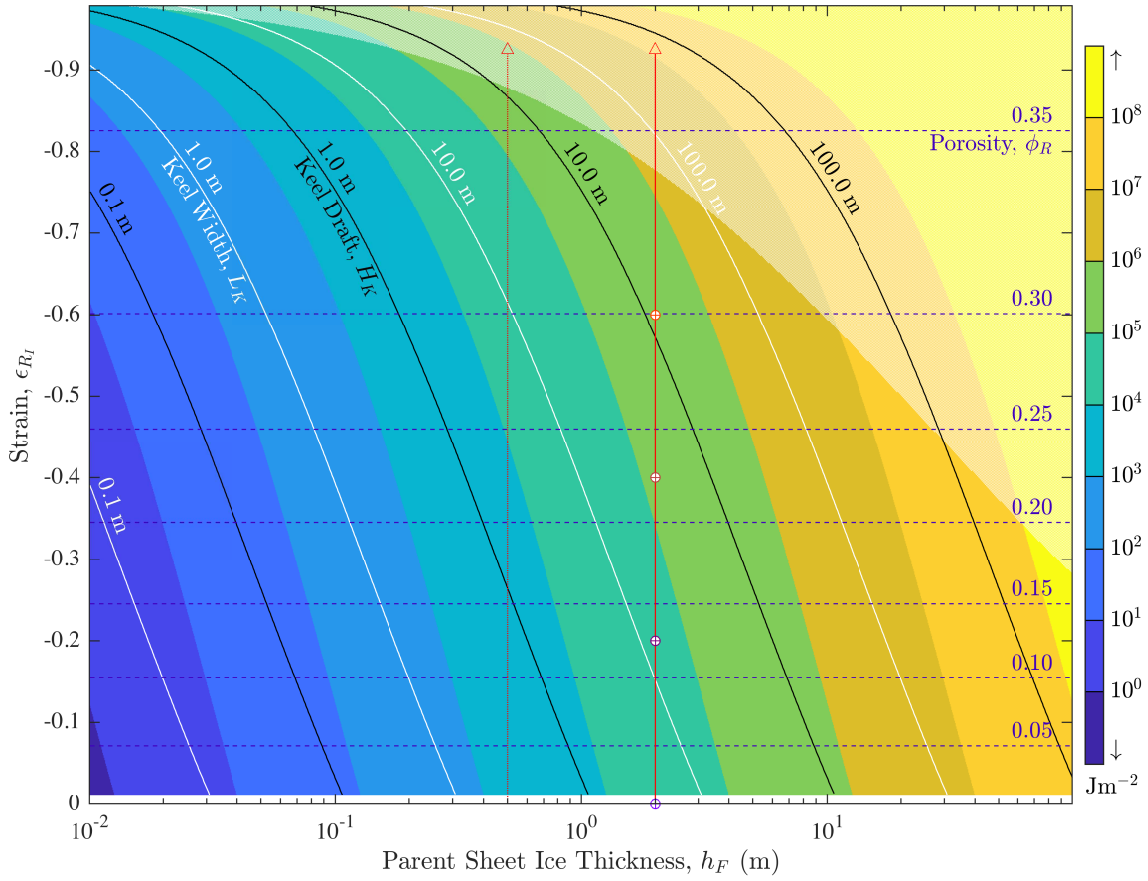

Figure 14. State space of ridged sea ice on the $\hat{\zeta}$-plane that passes through each $\hat{\zeta}$ trajectory on the $\mathcal{V}_R$=$\mathcal{V}(\epsilon_{R_I}, \phi_R, \hat{\alpha}_R, h_F)$ surfaces rendered in Figure 11. The state space is dependent only on initial ice thickness h_F and compressional strain ϵ_{R_I}. Color shading indicates potential energy density $\mathcal{V}_R$ of a ridge, for which there is a unique combination of keel width, L_K, keep draft, H_K, and porosity, ϕ_R, at every point on the $\hat{\zeta}$-plane. There is a corresponding angle of repose, α_K, sail height, H_S, and sail width, L_S, for each ridge state not shown here. Vertical red dashed and solid tracks correspond to $\hat{\zeta}$ trajectories in Figure 11 for h_F=0.5 and 2.0 m respectively, where colored markings on the latter correspond to $a_R(h, \phi_R, \boldsymbol{x})$ steps in Figure 13. Translucent shading indicates where the state space exceeds the *Tucker et al.* [1984] empirical $H_{S_{\max}}$ threshold discussed in section 0.8.

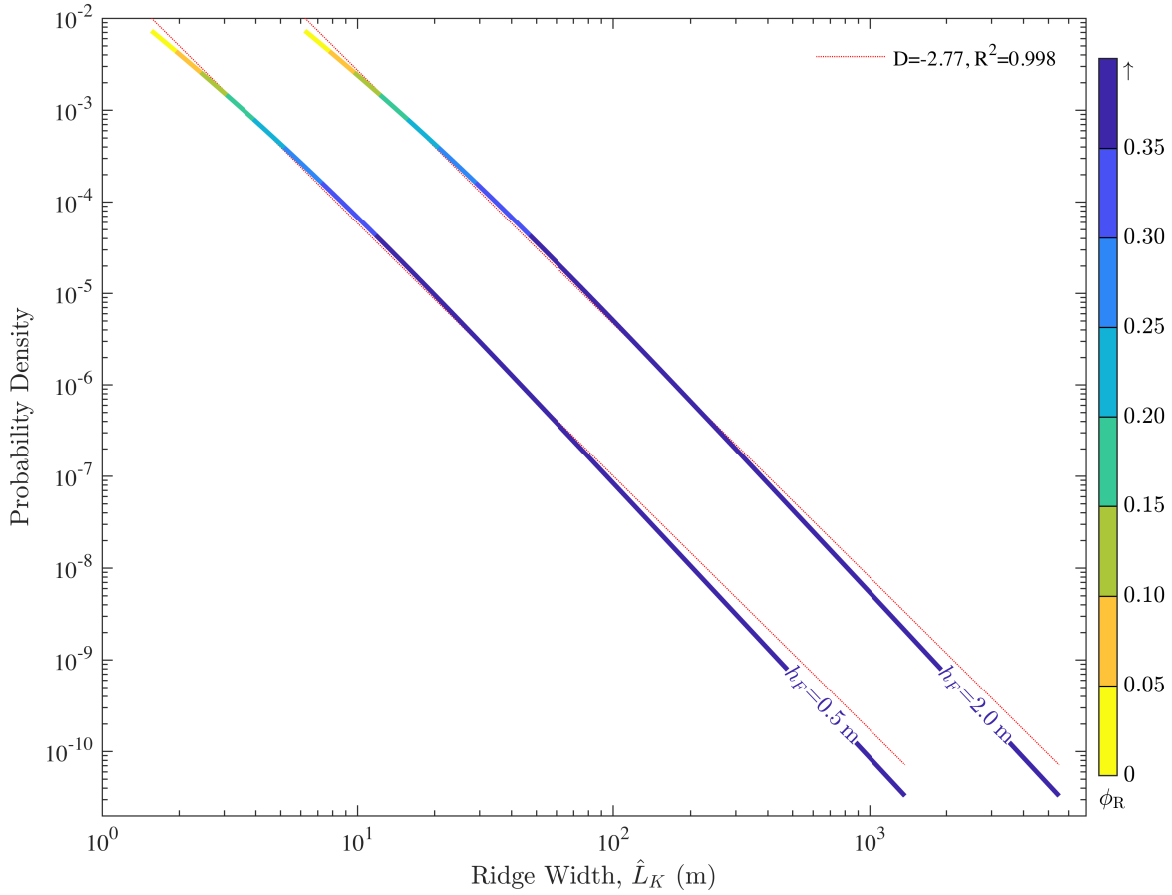

Figure 15. Probability density $b_R(h_F, \epsilon_{R_I})$ of ridges with cross-sectional width $\hat{L}_K$ occurring over an area A of uniform ice thickness h_F with 100% concentration for each of the two $\hat{\boldsymbol{\zeta}}$ trajectories illustrated for h_F=0.5 and 2.0 m in Figures 14 and 11. Color shading indicates the macroporosity for each probabilistic ridge state, and the dashed lines indicates the best linear fit for the relationship $b_R \propto \hat{L}_K^D$ with a corresponding R^2 value.

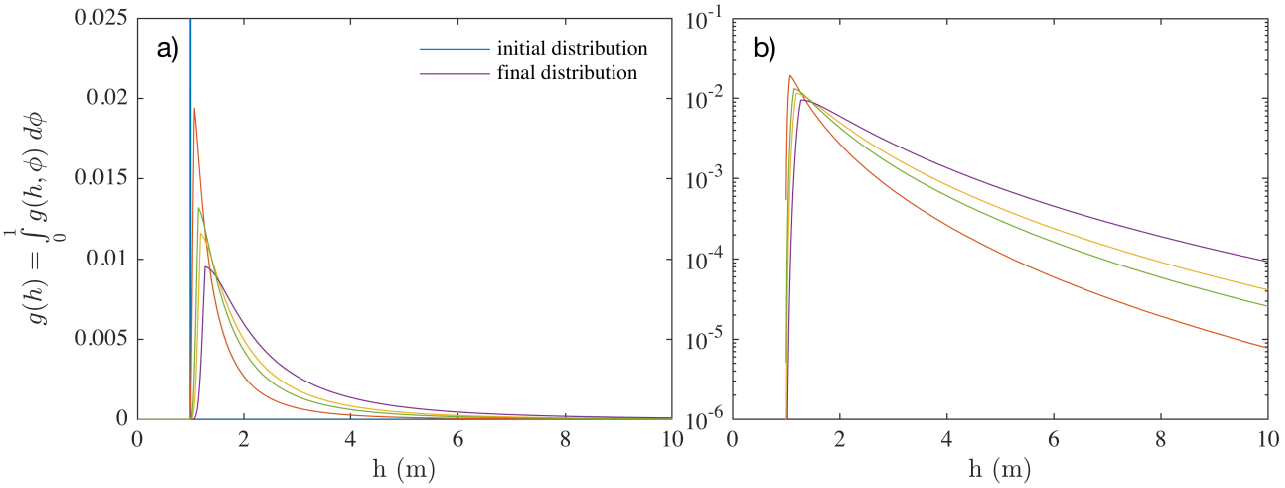

Figure 16. Integration of the sea ice conservation equation in (2) for an initially undeformed area of sea ice with uniform thickness h_F=1 m (blue). Selected iterative steps leading to the final distribution (purple) are shown for the integration procedure described in section 0.10. The graph in a) presents $g(h)$ on a linear y-axis, and b) presents the same $g(h)$ distribution on semilog axes so as to emphasize the near-negative exponential tail of the final distribution.